An extended macroscopic transport model for rarefied gas flows in long capillaries with circular cross section

Peyman Taheri[a] and Henning Struchtrup[b]
Department of Mechanical Engineering, University of Victoria, P.O. Box 3055, STN CSC, Victoria, British Columbia V8W 3P6, Canada

(Received 16 March 2010; accepted 5 September 2010; published online 30 November 2010)

Pressure-driven and thermally driven rarefied gas flows in long capillaries with circular cross sections are investigated. For both Poiseuille and thermal transpiration flows, a unified theoretical approach is presented based on the linear form of regularized 13-moment (R13) equations. The captured nonequilibrium effects in the processes are compared to available kinetic solutions, and the shortcomings of classical hydrodynamics, i.e., the Navier–Stokes–Fourier equations, are highlighted. Breakdown of Onsager's symmetry is proposed as a criterion to determine the range of applicability of extended macroscopic models. Based on Onsager's reciprocity relation it is shown that linearized R13 equations provide agreement with kinetic data for moderate Knudsen numbers, $\mathrm{Kn} \leq 0.25$. Two-way flow pattern and thermomolecular pressure difference in simultaneous pressure-driven and temperature-driven flows are analyzed. Moreover, second-order boundary conditions for velocity slip and temperature jump are derived for the Navier–Stokes–Fourier system. The proposed boundary conditions effectively improve classical hydrodynamics in the transition flow regime. © *2010 American Institute of Physics*. [doi:10.1063/1.3500681]

I. INTRODUCTION

The equations of classical continuum gas dynamics, i.e., the Navier–Stokes and Fourier laws, can describe gas flows except in a thin layer adjacent to the boundary, the Knudsen boundary layer. By increase of the Knudsen number Kn, the ratio of molecular mean free path to a geometric characteristic length of the flow, the thickness of the Knudsen layer increases. As a result, nonequilibrium effects dominate the flow and the classical Navier–Stokes–Fourier (NSF) system fails to accurately describe the flow.

Rarefied gas flows, regardless of their rarefaction degree, are precisely described by Boltzmann's kinetic equation.[1] Nevertheless, due to the complexity of the collision process and high dimensionality of the microscopic velocity field, solutions for the Boltzmann equation are computationally very expensive and still remain formidable.

Alternatively, macroscopic transport equations, which are deduced from the Boltzmann equation in a rational manner, can be used to describe rarefied gas flows to some extent of rarefaction degree. The Chapman–Enskog expansion[2] and Grad's moment expansion[3,4] are the classical methods to extract macroscopic transport equations from the Boltzmann kinetic equation. Among these, the method of moments has recently attracted a great deal of interest. This is due to its stability and also availability of boundary conditions for the moments. Indeed, Burnett-type equations obtained from the Chapman–Enskog method suffer from linear instabilities[5] and the lack of a unified strategy to construct the required boundary conditions.[6]

In the present work, the regularized 13-moment (R13) equations[7,8] and their corresponding boundary conditions[9] are employed to investigate nonequilibrium effects in Poiseuille and transpiration flows of rarefied gas flows in tubes. The R13 equations are the regularized version of the original Grad's 13-moment (G13) equations[3] and are applicable to dilute gas flows at early stages of the transition regime, i.e., $\mathrm{Kn} < 0.5$. In comparison to the G13 system, the R13 equations have shown superiority in describing shock structures,[10] Knudsen boundary layers, and nonequilibrium bulk effects.[9,11–15]

Tubes with circular cross section are favored in engineering applications as flow passages. Rarefied gas flows in circular channels under pressure gradients (cylindrical Poiseuille flow) and temperature gradients (cylindrical thermal transpiration/creep flow) are rigorously investigated through kinetic approaches, see Ref. 16 for an extensive bibliography. Kinetic solutions of cylindrical Poiseuille flow were first reported in 1966 by Cercignani and Sernagiotto,[17] followed by Ferziger's improvements.[18] They confirmed the presence of a minimum in the flow rate, which was previously observed in experiments by Knudsen.[19]

One year later, Sone and Yamamoto,[20] and Loyalka,[21] initiated kinetic approaches for thermally driven flows in cylindrical tubes. Temperature-driven flows occur in gases when nonuniform temperature distributions are applied in the flow boundaries. This type of flow was first reported by Reynolds[22] in 1879 who called it *thermal transpiration flow*. The interesting phenomenon in transpiration flows is the existence of a pumping effect, also known as thermomolecular pressure difference (TPD), which was proved by Knudsen experiments.[23]

Nowadays, owing to broad improvements in computational facilities and numerical schemes, the quality of kinetic

[a]Electronic mail: peymant@uvic.ca. Present address: Mechatronic Systems Engineering, School of Engineering Science, Simon Fraser University, British Columbia V3T 0A3, Canada.
[b]Electronic mail: struchtr@uvic.ca.

solutions for cylindrical Poiseuille and transpiration flows is considerably improved. Thus, they provide a reliable benchmark for validating the results of macroscopic approaches and even for calibrating the experiments.

We investigate steady state flows subject to small longitudinal pressure and temperature gradients, where the linearized R13 equations can be used to analyze the problem with minimum numerical effort. In order to validate our solutions, we compare them with the most recent kinetic data. Moreover, we present Navier–Stokes–Fourier solutions to highlight their shortcomings in describing nonequilibrium effects.

An explicit solution for two-way flow pattern, which appears in simultaneous Poiseuille and transpiration flows, is discussed. Furthermore, we examine the validity of Onsager's reciprocity relation for both NSF and R13 equations. Breakdown of Onsager's symmetry is used as a new criterion to determine the range of applicability of macroscopic approaches.

Finally, in order to improve the accuracy of classical NSF hydrodynamics, a new set of velocity slip and temperature jump conditions for Navier–Stokes–Fourier system is proposed. These conditions are deduced from the R13 kinetic boundary conditions using a scaling approach.[13,15] It is shown that these second-order boundary conditions for axial flows in tubes considerably improve the NSF solutions for the considered boundary value problems.

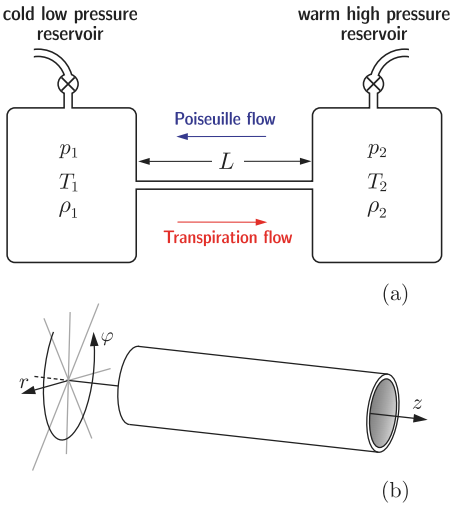

FIG. 1. (Color online) Poiseuille flow, thermal transpiration flow, and their combination are illustrated between two vessels (a), which are connected through a long pipe (b). In the case of pressure driven Poiseuille flow, a constant pressure difference is maintained between the reservoirs by adjusting the valves. In thermal transpiration flow a temperature gradient in axial z-direction is applied on the tube wall which connects the temperatures of two vessels. This longitudinal temperature gradient induces a flow from the cold reservoir to the warm one, while their pressure is the same. When the system is closed and a temperature gradient is applied on the tube wall, Poiseuille and transpiration flows occur simultaneously. In such a setting, temperature and pressure gradients have the same direction along the tube, but their corresponding flows have opposite directions.

II. STATEMENT OF THE PROBLEM

We consider a system including two reservoirs containing the same gas, joined by a capillary of length L, as depicted in Fig. 1(a). The pressure p, temperature T, and mass density ρ of the gas in the cold low-pressure and warm high-pressure reservoirs are denoted by $\{p_1,T_1,\rho_1\}$ and $\{p_2,T_2,\rho_2\}$, respectively, and the valves of reservoirs allow to adjust these conditions.

First, we assume isothermal reservoirs $T_1=T_2$, while a constant pressure difference is maintained between the reservoirs by adjusting the valves such that $p_2>p_1$. In this setting a pressure driven Poiseuille flow occurs from the right reservoir to the left one. Quite differently, a thermally induced flow can be initiated between isobaric reservoirs, $p_1=p_2$, which are kept at different temperatures $T_1>T_2$, and a temperature gradient along the capillary wall connects the temperatures of the reservoirs. In this setting the gas flows from the cold reservoir to the hot one. The arising flow is known as thermal creep flow or thermal transpiration flow.[24]

Furthermore, we consider simultaneous Poiseuille and transpiration flows in a closed system, i.e., when both valves are closed. Initially, we assume isobaric reservoirs with different temperatures and a temperature gradient along the capillary wall. This setting initiates a thermally driven flow in the tube in the direction of the temperature gradient. Therefore, a pressure difference between the reservoirs will establish, known as the thermomolecular pressure difference.[23,25] This, in turn, will induce a pressure driven Poiseuille flow, in the opposite direction of the transpiration flow. We emphasize that in such a flow setting temperature and pressure gradients have the same direction along the tube, while their corresponding flows have opposite directions. There will be a transpiration flow at the walls and a backward flow in the center of the pipe. After a sufficiently long time, a steady state condition will establish in which the closed reservoirs have constant pressure and temperature ratios, and the net mass flow in the capillary is zero. The relation between pressure and temperature can be presented by

$$\frac{p_2}{p_1}=\left(\frac{T_2}{T_1}\right)^{\gamma}, \tag{1}$$

where γ is the exponent of thermomolecular pressure difference,[16] which strongly depends on the degree of gas rarefaction,[25,26] i.e., the Knudsen number.

Throughout the following monatomic ideal gases are considered where $p=\rho\mathcal{R}T=\rho\theta$ is the equation of state. For simplicity, the temperature in energy units $\theta=\mathcal{R}T$ is defined, where $\mathcal{R}=k_B/m$ is the gas constant, with k_B and m as the Boltzmann constant and mass of the gas molecules, respectively. We investigate steady state flow in a long capillary with circular cross section of radius R, see Fig. 1(b). Thus, cylindrical coordinates $\mathbf{x}=\{r,\varphi,z\}$ are employed in our analysis, where r and z are the radial and axial coordinates, respectively. The flow is irrotational, $v_\varphi=0$, and independent of the azimuthal coordinate, i.e., $\partial/\partial\varphi=0$.

III. FLOW IN LONG TUBES

In general, due to compressibility effects, flow in the tube (cf. Fig. 1) is two-dimensional in the r-z plane, which requires a numerical approach. As discussed in Ref. 16, in flows through long passages one can safely discard the small

compressibility effects and describe the overall flow behavior using a one-dimensional transport field. In this section we use the same approach which is used in Ref. 16 to justify the unidirectional flow assumption in long tubes.

For sufficiently long tubes where $L/R=\ell \gg 1$, one can assume that density and temperature variations in the cross section are negligible compared to their longitudinal variation, so that $\rho=\rho(z)$ and $\theta=\theta(z)$. To proceed, we choose the radius of the tube as the reference length scale to define the dimensionless coordinates

$$\tilde{r}=\frac{r}{R} \quad \text{and} \quad \tilde{z}=\frac{z}{R}. \tag{2}$$

Indeed, the reservoirs affect the flow at the capillary ends, but compared to the length of the capillary, the entry/exit effects are limited to very small regions. Then, ignoring these effects,[27] we have

$$\rho(0)=\rho_1, \quad \rho(\ell)=\rho_2, \quad \theta(0)=\theta_1, \quad \theta(\ell)=\theta_2. \tag{3}$$

At any arbitrary cross section $\tilde{z}=\tilde{z}_0$ along the tube and for $|\tilde{z}-\tilde{z}_0|\lesssim 1$ we can write

$$\rho(\tilde{z})=\rho(\tilde{z}_0)+\left.\frac{\partial\rho}{\partial\tilde{z}}\right|_{\tilde{z}=\tilde{z}_0}(\tilde{z}-\tilde{z}_0)+\frac{1}{2}\left.\frac{\partial^2\rho}{\partial\tilde{z}^2}\right|_{\tilde{z}=\tilde{z}_0}(\tilde{z}-\tilde{z}_0)^2+\cdots,$$
$$\theta(\tilde{z})=\theta(\tilde{z}_0)+\left.\frac{\partial\theta}{\partial\tilde{z}}\right|_{\tilde{z}=\tilde{z}_0}(\tilde{z}-\tilde{z}_0)+\frac{1}{2}\left.\frac{\partial^2\theta}{\partial\tilde{z}^2}\right|_{\tilde{z}=\tilde{z}_0}(\tilde{z}-\tilde{z}_0)^2+\cdots. \tag{4}$$

The order of derivations can be expressed in terms of the smallness parameter $1/\ell$,

$$\frac{\partial\rho}{\partial\tilde{z}}\sim\frac{\rho_1-\rho_2}{\ell}=\mathcal{O}\left(\frac{1}{\ell}\right), \quad \frac{\partial^2\rho}{\partial\tilde{z}^2}\sim\frac{\rho_1-\rho_2}{\ell^2}=\mathcal{O}\left(\frac{1}{\ell^2}\right),$$
$$\frac{\partial\theta}{\partial\tilde{z}}\sim\frac{\theta_1-\theta_2}{\ell}=\mathcal{O}\left(\frac{1}{\ell}\right), \quad \frac{\partial^2\theta}{\partial\tilde{z}^2}\sim\frac{\theta_1-\theta_2}{\ell^2}=\mathcal{O}\left(\frac{1}{\ell^2}\right). \tag{5}$$

Since $\ell\gg 1$, the second-order derivatives can be neglected, and the expansions in Eq. (4) reduce to

$$\rho(\tilde{z})=\rho_0[1+\varrho(\tilde{z}-\tilde{z}_0)] \quad \text{and} \quad \theta(\tilde{z})=\theta_0[1+\tau(\tilde{z}-\tilde{z}_0)], \tag{6}$$

with

$$\rho_0=\rho(\tilde{z}_0), \quad \varrho=\left.\frac{\partial(\rho/\rho_0)}{\partial\tilde{z}}\right|_{\tilde{z}=\tilde{z}_0}=\mathcal{O}\left(\frac{1}{\ell}\right),$$
$$\theta_0=\theta(\tilde{z}_0), \quad \tau=\left.\frac{\partial(\theta/\theta_0)}{\partial\tilde{z}}\right|_{\tilde{z}=\tilde{z}_0}=\mathcal{O}\left(\frac{1}{\ell}\right). \tag{7}$$

Accordingly, we can conclude that near a given cross section, $\tilde{z}_0$, on a distance of the order of the tube radius R, density and temperature linearly vary with respect to $\tilde{z}$, and their gradients are small constants of order $(1/\ell)$. Replacement of density and temperature from Eq. (6) into the ideal gas law gives

$$p(\tilde{z})=p_0[1+\wp(\tilde{z}-\tilde{z}_0)],$$

with

$$p_0=\rho_0\theta_0, \quad \wp=\varrho+\tau=\left.\frac{\partial(p/p_0)}{\partial\tilde{z}}\right|_{\tilde{z}=\tilde{z}_0}=\mathcal{O}\left(\frac{1}{\ell}\right), \tag{8}$$

again, all terms of order $(\tilde{z}-\tilde{z}_0)^2$ are neglected due to linearization.

The constant pressure and temperature gradients are the driving forces for the Poiseuille and transpiration flows, respectively. As will be shown in Sec. VI, our linear analysis discards axial compressibility effects and allows to simplify the problem such that a one-dimensional analysis can be employed to investigate the local transport field across the tube.

The tube walls are impermeable and there is no velocity in the radial direction, $v_r=0$. Since the flow is assumed to be independent of the φ-direction, the velocity vector $\mathbf{v}$, the heat-flux vector $\mathbf{q}$, and the symmetric and trace-free stress tensor $\boldsymbol{\sigma}$ simplify to

$$\mathbf{v}=\begin{pmatrix}0\\0\\v_z(r)\end{pmatrix}, \quad \mathbf{q}=\begin{pmatrix}q_r(r)\\0\\q_z(r)\end{pmatrix},$$
$$\boldsymbol{\sigma}=\begin{pmatrix}\sigma_{rr}(r) & 0 & \sigma_{rz}(r)\\ 0 & \sigma_{\varphi\varphi}(r) & 0\\ \sigma_{rz}(r) & 0 & \sigma_{zz}(r)\end{pmatrix}, \tag{9}$$

where all components are only functions of the radial coordinate r. Trace-free condition for the stress tensor gives $\sigma_{\varphi\varphi}(r)=-\sigma_{rr}(r)-\sigma_{zz}(r)$.

IV. FULL R13 EQUATIONS

The core equations in the R13 system are the conservation laws for mass, momentum, and energy, which at steady state condition and for the proposed geometry (cf. Fig. 1) reduce to

$$\frac{\partial p}{\partial r}+\frac{\partial\sigma_{rr}}{\partial r}+\frac{2\sigma_{rr}+\sigma_{zz}}{r}=0, \tag{10}$$

$$\frac{\partial\sigma_{rz}}{\partial r}+\frac{\sigma_{rz}}{r}=-\frac{\partial p}{\partial z}, \tag{11}$$

$$\frac{\partial q_r}{\partial r}+\frac{q_r}{r}=-\sigma_{rz}\frac{\partial v_z}{\partial r}. \tag{12}$$

Equations (10) and (11) are the components of the momentum balance in the radial and axial directions, respectively. Referring to our linear analysis, the axial pressure gradient $\partial p/\partial z$ on the right-hand side of Eq. (11) is a small constant, which can be considered as a body force. Equation (12) is the energy balance, where the coupling between stress σ_{rz} and shear rate $\partial v_z/\partial r$ on the right-hand side describes viscous dissipation. Due to the prescribed geometry, continuity and φ-momentum equations are automatically satisfied.

The extended balance equations for the components of the stress tensor $\{\sigma_{rr},\sigma_{rz},\sigma_{zz}\}$ and heat-flux vector $\{q_r,q_z\}$

follow from their respective moment equations.[7,8,10,28] In cylindrical space coordinates, for the considered geometry (Fig. 1) they read

$$\frac{4}{15}\left(2\frac{\partial q_r}{\partial r}-\frac{q_r}{r}\right)-\frac{2}{3}\sigma_{rz}\frac{\partial v_z}{\partial r}+\frac{\partial m_{rrr}}{\partial r}+\frac{m_{rrr}-2m_{r\varphi\varphi}}{r}=-\frac{p}{\mu}\sigma_{rr}, \tag{13}$$

$$\frac{2}{5}\frac{\partial q_z}{\partial r}+\sigma_{rr}\frac{\partial v_z}{\partial r}+\frac{\partial m_{rrz}}{\partial r}+\frac{m_{rrz}-m_{\varphi\varphi z}}{r}=\underline{-\frac{p}{\mu}\sigma_{rz}-p\frac{\partial v_z}{\partial r}}, \tag{14}$$

$$-\frac{4}{15}\left(\frac{\partial q_r}{\partial r}+\frac{q_r}{r}\right)+\frac{4}{3}\sigma_{rz}\frac{\partial v_z}{\partial r}+\frac{\partial m_{rzz}}{\partial r}+\frac{m_{rzz}}{r}=-\frac{p}{\mu}\sigma_{zz}, \tag{15}$$

and

$$\begin{aligned}&\frac{7}{2}\sigma_{rr}\frac{\partial\theta}{\partial r}-\frac{\sigma_{rz}}{\rho}\left(\frac{\partial\sigma_{rz}}{\partial r}+\frac{\sigma_{rz}}{r}\right)+\theta\left(\frac{\partial\sigma_{rr}}{\partial r}+\frac{2\sigma_{rr}+\sigma_{zz}}{r}\right)\\&\quad+\frac{2}{5}q_z\frac{\partial v_z}{\partial r}+\frac{1}{2}\left(\frac{\partial R_{rr}}{\partial r}+\frac{2R_{rr}+R_{zz}}{r}\right)+\frac{1}{6}\frac{\partial\Delta}{\partial r}+m_{rrz}\frac{\partial v_z}{\partial r}\\&=\underline{-\Pr\frac{p}{\mu}q_r-\frac{5}{2}p\frac{\partial\theta}{\partial r}},\end{aligned} \tag{16}$$

$$\begin{aligned}&\frac{7}{2}\sigma_{rz}\frac{\partial\theta}{\partial r}+\left(\theta-\frac{\sigma_{zz}}{\rho}\right)\left(\frac{\partial\sigma_{rz}}{\partial r}+\frac{\sigma_{rz}}{r}\right)+\frac{7}{5}q_r\frac{\partial v_z}{\partial r}\\&\quad+\frac{1}{2}\left(\frac{\partial R_{rz}}{\partial r}+\frac{R_{rz}}{r}\right)+m_{rzz}\frac{\partial v_z}{\partial r}=\underline{-\Pr\frac{p}{\mu}q_z-\frac{5}{2}p\frac{\partial\theta}{\partial z}}.\end{aligned} \tag{17}$$

The underlined terms on the right-hand side of Eqs. (14), (16), and (17) represent the Navier–Stokes and Fourier laws of classical hydrodynamics, i.e., Newtonian viscous shear and Fourier's heat conduction. Viscosity of the gas is denoted by μ, and $\Pr=(5/2)(\mu/\kappa)$ is the Prandtl number, where κ is the thermal conductivity coefficient.

The axial temperature gradient $\partial\theta/\partial z$ in Eq. (17) is the driving force for thermal transpiration flow along the capillary; for the applications in this paper it is considered to be a small constant. Note that Eqs. (13)–(17) can be further simplified by means of the main conservation laws [cf. Eqs. (10)–(12)], but to keep some generality we proceed with the presented form.

While in Grad's original 13-moment system the higher–order moments $\{\Delta, R_{ij}, m_{ijk}\}$ are zero, the regularization procedure[7,28] gives these additional moments as

$$\begin{aligned}\Delta=A_1\frac{2(\sigma_{rr}^2+\sigma_{rz}^2+\sigma_{zz}^2+\sigma_{rr}\sigma_{zz})}{\rho}+A_2\frac{\mu}{p}\Bigg[\theta\left(\frac{\partial q_r}{\partial r}+\frac{q_r}{r}\right)\\+q_r\left(\frac{5}{2}\frac{\partial\theta}{\partial r}-\frac{\theta}{\rho}\frac{\partial\rho}{\partial r}\right)+\theta\sigma_{rz}\frac{\partial v_z}{\partial r}\Bigg],\end{aligned} \tag{18}$$

$$\begin{aligned}R_{rr}=\frac{B_1}{3}\frac{\sigma_{rr}^2+\sigma_{rz}^2-2\sigma_{zz}^2-2\sigma_{rr}\sigma_{zz}}{\rho}+\frac{B_2}{3}\frac{\mu}{p}\Bigg[\theta\left(2\frac{\partial q_r}{\partial r}-\frac{q_r}{r}\right)\\+2q_r\left(\frac{\partial\theta}{\partial r}-\frac{\theta}{\rho}\frac{\partial\rho}{\partial r}\right)+\frac{5}{7}\theta\sigma_{rz}\frac{\partial v_z}{\partial r}\Bigg],\end{aligned} \tag{19}$$

$$\begin{aligned}R_{rz}=B_1\frac{\sigma_{rz}(\sigma_{rr}+\sigma_{zz})}{\rho}+\frac{B_2}{2}\frac{\mu}{p}\Bigg[\theta\frac{\partial q_z}{\partial r}+q_z\left(\frac{\partial\theta}{\partial r}-\frac{\theta}{\rho}\frac{\partial\rho}{\partial r}\right)\\+\frac{5}{7}\theta(\sigma_{rr}+\sigma_{zz})\frac{\partial v_z}{\partial r}\Bigg],\end{aligned} \tag{20}$$

$$\begin{aligned}R_{zz}=\frac{B_1}{3}\frac{\sigma_{rz}^2+\sigma_{zz}^2-2\sigma_{rr}^2-2\sigma_{rr}\sigma_{zz}}{\rho}+\frac{B_2}{3}\frac{\mu}{p}\Bigg[-\theta\left(\frac{\partial q_r}{\partial r}+\frac{q_r}{r}\right)\\-q_r\left(\frac{\partial\theta}{\partial r}-\frac{\theta}{\rho}\frac{\partial\rho}{\partial r}\right)+\frac{5}{7}\theta\sigma_{rz}\frac{\partial v_z}{\partial r}\Bigg],\end{aligned} \tag{21}$$

$$\begin{aligned}m_{rrr}=C\frac{\mu}{p}\Bigg[\theta\left(\frac{3}{5}\frac{\partial\sigma_{rr}}{\partial r}-\frac{2}{5}\frac{2\sigma_{rr}+\sigma_{zz}}{r}\right)-\frac{3}{5}\frac{\theta\sigma_{rr}}{\rho}\frac{\partial\rho}{\partial r}\\-\frac{4}{25}q_z\frac{\partial v_z}{\partial r}\Bigg],\end{aligned} \tag{22}$$

$$\begin{aligned}m_{r\varphi\varphi}=C\frac{\mu}{p}\Bigg[\theta\left(-\frac{7}{15}\frac{\partial\sigma_{rr}}{\partial r}-\frac{1}{3}\frac{\partial\sigma_{zz}}{\partial r}+\frac{8}{15}\frac{2\sigma_{rr}+\sigma_{zz}}{r}\right)\\-\frac{1}{3}\frac{\theta}{\rho}\left(\sigma_{\varphi\varphi}-\frac{2}{5}\sigma_{rr}\right)\frac{\partial\rho}{\partial r}-\frac{4}{75}q_z\frac{\partial v_z}{\partial r}\Bigg],\end{aligned} \tag{23}$$

$$\begin{aligned}m_{\varphi\varphi z}=C\frac{\mu}{p}\Bigg[\theta\left(-\frac{2}{15}\frac{\partial\sigma_{rz}}{\partial r}+\frac{8}{15}\frac{\sigma_{rz}}{r}\right)+\frac{2}{15}\frac{\theta\sigma_{rz}}{\rho}\frac{\partial\rho}{\partial r}\\-\frac{4}{75}q_r\frac{\partial v_z}{\partial r}\Bigg],\end{aligned} \tag{24}$$

$$m_{rrz}=C\frac{\mu}{p}\left[\theta\left(\frac{8}{15}\frac{\partial\sigma_{rz}}{\partial r}-\frac{2}{15}\frac{\sigma_{rz}}{r}\right)-\frac{8}{15}\frac{\theta\sigma_{rz}}{\rho}\frac{\partial\rho}{\partial r}+\frac{16}{75}q_r\frac{\partial v_z}{\partial r}\right], \tag{25}$$

$$\begin{aligned}m_{rzz}=C\frac{\mu}{p}\Bigg[\theta\left(\frac{1}{3}\frac{\partial\sigma_{zz}}{\partial r}-\frac{2}{15}\frac{\partial\sigma_{rr}}{\partial r}-\frac{2}{15}\frac{2\sigma_{rr}+\sigma_{zz}}{r}\right)\\-\frac{1}{3}\frac{\theta}{\rho}\left(\sigma_{zz}-\frac{2}{5}\sigma_{rr}\right)\frac{\partial\rho}{\partial r}+\frac{16}{75}q_z\frac{\partial v_z}{\partial r}\Bigg].\end{aligned} \tag{26}$$

The coefficients $\{A_n, B_n, C\}$ in Eqs. (16)–(26) depend on the underlying kinetic model. Their derivation from the Boltzmann equation (BE) gives[28]

$$\Pr^{\mathrm{BE}}=\frac{2}{3},\quad A_1^{\mathrm{BE}}=-1,\quad A_2^{\mathrm{BE}}=-12,$$
$$B_1^{\mathrm{BE}}=-\frac{4}{7},\quad B_2^{\mathrm{BE}}=-\frac{24}{5},\quad C^{\mathrm{BE}}=-2, \tag{27}$$

while the Bhatnagar–Gross–Krook (BGK) kinetic model gives their value as[28]

$$\Pr^{\mathrm{BGK}}=1,\quad A_1^{\mathrm{BGK}}=0,\quad A_2^{\mathrm{BGK}}=-8,$$
$$B_1^{\mathrm{BGK}}=0,\quad B_2^{\mathrm{BGK}}=-\frac{28}{5},\quad C^{\mathrm{BGK}}=-3. \tag{28}$$

As indicated by the underlined terms in Eqs. (14), (16), and (17), in classical hydrodynamics, heat flow and stress are

proportional to the gradients of temperature and velocity, respectively. In the prescribed geometry (Fig. 1), the laws of Fourier and Navier–Stokes are

$$q_r^{\mathrm{NSF}} = -\frac{5}{2}\frac{\mu}{\mathrm{Pr}}\frac{\partial\theta}{\partial r} \quad \text{and} \quad q_z^{\mathrm{NSF}} = -\frac{5}{2}\frac{\mu}{\mathrm{Pr}}\frac{\partial\theta}{\partial z}, \tag{29}$$

and

$$\sigma_{rz}^{\mathrm{NSF}} = -\mu\frac{\partial v_z}{\partial r} \quad \text{and} \quad \sigma_{rr}^{\mathrm{NSF}} = \sigma_{zz}^{\mathrm{NSF}} = 0. \tag{30}$$

V. BOUNDARY CONDITIONS

From experimental observations and theoretical considerations it is well known that gas flows slip over the bounding surfaces. Moreover, a temperature jump appears at the gas-surface interface, when nonisothermal flows are considered. The magnitude of slip and jump is proportional to the Knudsen number.[1,24]

In the NSF theory with $\{\rho, \mathbf{v}, \theta\}$ as its primary quantities, discontinuity conditions for velocity and temperature suffice to solve boundary value problems. However, for extended systems such as R13, where $\{\rho, \mathbf{v}, \theta, \mathbf{q}, \boldsymbol{\sigma}\}$ are the primary variables, additional discontinuity conditions for the higher-order moments $\{\mathbf{q}, \boldsymbol{\sigma}\}$ are required.

A. Kinetic boundary conditions for regularized 13-moment equations

Recently, Maxwell's boundary condition[29] for the Boltzmann equation has been successfully applied to obtain macroscopic boundary conditions for high-order moments.[9,30] The full set of boundary conditions for the flows depicted in Fig. 1 is[9]

$$\sigma_{rz} = \frac{-\chi}{2-\chi}\sqrt{\frac{2}{\pi\theta}}\left(\mathcal{P}\mathcal{V}_z + \frac{1}{5}q_z + \frac{1}{2}m_{rrz}\right)n_r, \tag{31a}$$

$$R_{rz} = \frac{\chi}{2-\chi}\sqrt{\frac{2}{\pi\theta}}\left(\mathcal{P}\mathcal{V}_z(\theta - \mathcal{V}^2 + 6\mathcal{T}) - \frac{11}{5}\theta q_z - \frac{1}{2}\theta m_{rrz}\right)n_r, \tag{31b}$$

$$q_r = \frac{-\chi}{2-\chi}\sqrt{\frac{2}{\pi\theta}}\left(2\mathcal{P}\mathcal{T} - \frac{1}{2}\mathcal{P}\mathcal{V}^2 + \frac{1}{2}\theta\sigma_{rr} + \frac{1}{15}\Delta + \frac{5}{28}R_{rr}\right)n_r, \tag{31c}$$

$$m_{rrr} = \frac{\chi}{2-\chi}\sqrt{\frac{2}{\pi\theta}}\left(\frac{2}{5}\mathcal{P}\mathcal{T} - \frac{3}{5}\mathcal{P}\mathcal{V}^2 - \frac{7}{5}\theta\sigma_{rr} + \frac{1}{75}\Delta - \frac{1}{14}R_{rr}\right)n_r, \tag{31d}$$

$$m_{rzz} = \frac{-\chi}{2-\chi}\sqrt{\frac{2}{\pi\theta}}\left(\frac{1}{5}\mathcal{P}\mathcal{T} - \frac{4}{5}\mathcal{P}\mathcal{V}^2 + \frac{1}{14}R_{zz} + \theta\left(\sigma_{zz} - \frac{1}{5}\sigma_{rr}\right) + \frac{1}{150}\Delta\right)n_r, \tag{31e}$$

with

$$\mathcal{P} = p + \frac{1}{2}\sigma_{rr} - \frac{1}{120}\frac{\Delta}{\theta} - \frac{1}{28}\frac{R_{rr}}{\theta}, \qquad \mathcal{V}_z = v_z - v_z^W, \quad \mathcal{T} = \theta - \theta_W. \tag{32}$$

Here, $\mathcal{V}_z$ and $\mathcal{T}$ denote slip velocity and temperature jump at the wall, respectively, with the sub/superscript "W" referring to the properties of the tube wall. The wall normal n_r points in radial direction toward the gas, thus $n_r = -1$. The surface accommodation factor is denoted by χ, where $\chi = 0$ and $\chi = 1$ represent fully reflective (smooth) and fully diffusive (rough) walls, respectively.

In a steady state flow, the mass of the gas in the tube is constant. This can be used as an auxiliary condition to find the density distribution in the tube cross section. For a unit length of tube, $\Delta z = 1$, this condition reads

$$\int_{z_0}^{z_0+1}\int_0^{2\pi}\int_0^R \rho(r) r dr d\varphi dz = M_0, \tag{33}$$

where M_0 is the mass of the gas.

B. Second-order boundary conditions for NSF equations

From the viewpoint of the Chapman–Enskog expansion method[2] the R13 boundary conditions in Eqs. (31a)–(31e) include a range of first-, second-, and third-order moments (in terms of presence of the Knudsen number). Therefore, they can be used to derive high-order slip velocity and temperature jump conditions for the NSF equations. The strategy to obtain these high-order conditions is presented in Ref. 13, and it is utilized here to find second-order contributions of high-order moments to slip velocity and temperature jump in cylindrical geometry; details are presented in Appendix A.

For the linearized Boltzmann kinetic model with the coefficients given in Eq. (27), the slip condition reads

$$\mathcal{V}_z^{\text{NSF-BE}} = -\frac{\frac{2-\chi}{\chi}\sqrt{\frac{\pi\theta}{2}}\frac{\sigma_{rz}^{\mathrm{NSF}}}{p}n_r + \underline{\frac{3}{4}\frac{\mu}{p}\frac{\partial\theta}{\partial z}} - \frac{19}{18}\frac{q_r^{\mathrm{NSF}}\sigma_{rz}^{\mathrm{NSF}}}{p^2}}{+\frac{1}{6}\frac{\mu\theta}{p^2}\left(5\frac{\partial}{\partial r} + \frac{1}{r}\right)\sigma_{rz}^{\mathrm{NSF}}}, \tag{34}$$

while for the BGK model with coefficients (28) it becomes

$$\mathcal{V}_z^{\text{NSF-BGK}} = -\frac{\frac{2-\chi}{\chi}\sqrt{\frac{\pi\theta}{2}}\frac{\sigma_{rz}^{\mathrm{NSF}}}{p}n_r + \underline{\frac{1}{2}\frac{\mu}{p}\frac{\partial\theta}{\partial z}} - \frac{6}{5}\frac{q_r^{\mathrm{NSF}}\sigma_{rz}^{\mathrm{NSF}}}{p^2}}{+\frac{\mu\theta}{p^2}\frac{\partial\sigma_{rz}^{\mathrm{NSF}}}{\partial r}}. \tag{35}$$

Analogously, the jump conditions for temperature are obtained as

$$\mathcal{T}^{\text{NSF-BE}} = -\frac{2-\chi}{\chi}\sqrt{\frac{\pi\theta}{2}}\frac{q_r^{\text{NSF}}}{2p}n_r + \frac{2}{35}\frac{\mu\theta}{p^2}\left(12\frac{\partial}{\partial r}+\frac{1}{r}\right)q_r^{\text{NSF}} - \frac{92}{175}\frac{(q_r^{\text{NSF}})^2}{p^2} + \left[\left(\frac{2-\chi}{\chi}\right)^2\frac{\pi}{8}-\frac{29}{245}\right]\frac{\theta}{p^2}(\sigma_{rz}^{\text{NSF}})^2 \tag{36}$$

and

$$\mathcal{T}^{\text{NSF-BGK}} = -\frac{2-\chi}{\chi}\sqrt{\frac{\pi\theta}{2}}\frac{q_r^{\text{NSF}}}{2p}n_r + \frac{1}{10}\frac{\mu\theta}{p^2}\left(6\frac{\partial}{\partial r}-\frac{1}{r}\right)q_r^{\text{NSF}} - \frac{16}{25}\frac{(q_r^{\text{NSF}})^2}{p^2} + \left[\left(\frac{2-\chi}{\chi}\right)^2\frac{\pi}{8}-\frac{3}{35}\right]\frac{\theta}{p^2}(\sigma_{rz}^{\text{NSF}})^2. \tag{37}$$

In Eqs. (34)–(37) the quantities q_r^{NSF} and σ_{rz}^{NSF} denote heat flux and stress according to the Fourier and Navier–Stokes laws [cf. Eqs. (29) and (30)]. The underlined terms indicate the first-order slip velocity and temperature jump contributions, while the rest are second-order corrections. The double-underlined terms are applicable only for the thermal transpiration flow as they take account for the effects of longitudinal temperature gradients.

VI. DIMENSIONLESS AND LINEARIZED EQUATIONS

Equations (10)–(26) describe the radial distribution of flow properties in the presence of constant pressure and temperature gradients. In low speed rarefied gas flows, which are subject to small density and temperature gradients, Eqs. (10)–(26) in their linear form can be employed to describe the flow. To present linear equations the local reference equilibrium state $\{\rho_0, \theta_0, v_i^0\}$ at $z=z_0$ is employed.

The following linearized equations are presented in dimensionless form. The dimensionless axial and radial coordinates are defined in Eq. (2), where the radius of the tube, R, is used as the reference length scale. Dimensionless mass density, temperature, and pressure are defined as their deviations from the local reference state,

$$\frac{\rho}{\rho_0} = 1+\tilde{\rho}, \quad \frac{\theta}{\theta_0} = 1+\tilde{\theta}, \quad \text{and} \quad \frac{p}{p_0} = 1+\tilde{p} = 1+\tilde{\rho}+\tilde{\theta}. \tag{38}$$

The local thermal speed, $\sqrt{\theta_0}$, and reference density, ρ_0, are used to define the remaining dimensionless quantities,

$$\tilde{v}_i = \frac{v_i}{\sqrt{\theta_0}}, \quad \tilde{\sigma}_{ij} = \frac{\sigma_{ij}}{\rho_0\theta_0}, \quad \tilde{q}_i = \frac{q_i}{\rho_0\sqrt{\theta_0}^3}, \quad \tilde{\Delta} = \frac{\Delta}{\rho_0\theta_0^2}, \quad \tilde{R}_{ij} = \frac{R_{ij}}{\rho_0\theta_0^2}, \quad \tilde{m}_{ijk} = \frac{m_{ijk}}{\rho_0\sqrt{\theta_0}^3}. \tag{39}$$

Furthermore, $\mu/\mu_0 = 1+\tilde{\mu}$ is the dimensionless viscosity with $\mu_0=\mu(\theta_0)$. Dimensionless deviations vanish in the reference equilibrium state. In the following dimensionless and linearized equations, viscosity appears through the Knudsen number Kn, defined as the ratio of mean free path λ to the characteristic length scale $\mathcal{L}$,

$$\text{Kn} = \frac{\lambda_0}{\mathcal{L}} = \frac{\mu_0\sqrt{\theta_0}}{p_0 R}. \tag{40}$$

Here $\lambda_0=\mu_0\sqrt{\theta_0}/p_0$ is the molecular mean free path in the reference equilibrium state and the radius of the tube R is chosen as the reference length.

Linearization leads to decoupling of equations, such that Eqs. (10)–(26) and their corresponding boundary conditions (31a)–(31e) can be separated into the following three sets of ordinary differential equations.

(i) The velocity problem.

R13 case. In the linear case, to find the gas velocity we need to solve the following subset of equations:

$$\left(\frac{\partial}{\partial\tilde{r}}+\frac{1}{\tilde{r}}\right)\tilde{\sigma}_{rz} = -\wp, \tag{41a}$$

$$-\wp+\frac{1}{2}\left(\frac{\partial}{\partial\tilde{r}}+\frac{1}{\tilde{r}}\right)\tilde{R}_{rz} = -\frac{\text{Pr}}{\text{Kn}}\tilde{q}_z-\frac{5}{2}\tau, \tag{41b}$$

$$\frac{2}{5}\frac{\partial\tilde{q}_z}{\partial\tilde{r}}+\frac{\partial\tilde{m}_{rrz}}{\partial\tilde{r}}+\frac{\tilde{m}_{rrz}-\tilde{m}_{\varphi\varphi z}}{\tilde{r}} = -\frac{1}{\text{Kn}}\tilde{\sigma}_{rz}-\frac{\partial\tilde{v}_z}{\partial\tilde{r}}, \tag{41c}$$

with the constitutive relations

$$\tilde{R}_{rz} = \frac{1}{2}B_2\,\text{Kn}\frac{\partial\tilde{q}_z}{\partial\tilde{r}}, \quad \tilde{m}_{rrz} = -\frac{8}{15}C\,\text{Kn}\left(\wp+\frac{5}{4}\frac{\tilde{\sigma}_{rz}}{\tilde{r}}\right), \quad \tilde{m}_{\varphi\varphi z} = \frac{2}{15}C\,\text{Kn}\left(\wp+5\frac{\tilde{\sigma}_{rz}}{\tilde{r}}\right), \tag{42}$$

and the linearized boundary conditions

$$\tilde{\sigma}_{rz} = \frac{-\chi}{2-\chi}\sqrt{\frac{2}{\pi}}\left(\tilde{v}_z+\frac{1}{5}\tilde{q}_z+\frac{1}{2}\tilde{m}_{rrz}\right)n_r, \tag{43a}$$

$$\tilde{R}_{rz} = \frac{\chi}{2-\chi}\sqrt{\frac{2}{\pi}}\left(\tilde{v}_z-\frac{11}{5}\tilde{q}_z-\frac{1}{2}\tilde{m}_{rrz}\right)n_r. \tag{43b}$$

Equation (41a) is the dimensionless and linearized axial momentum balance [cf. Eq. (11)], $\wp=\partial\tilde{p}/\partial\tilde{z}$ was introduced in Eq. (8). Also, Eq. (41b) is the dimensionless and linearized axial heat-flux balance [cf. Eq. (17)] with $\tau=\partial\tilde{\theta}/\partial\tilde{z}$, as the constant and dimensionless axial temperature gradient [Eq. (6)]. Equation (41c) is the dimensionless and linear form of the shear-stress balance.

Navier–Stokes–Fourier case. In the hydrodynamic limit, where high-order moments vanish, the velocity problem consists of axial momentum balance and axial heat-flux balance [Eqs. (41a) and (41b)],

$$\left(\frac{\partial}{\partial\tilde{r}}+\frac{1}{\tilde{r}}\right)\frac{\partial\tilde{v}_z}{\partial\tilde{r}} = \frac{\wp}{\text{Kn}}, \quad 0 = -\frac{\text{Pr}}{\text{Kn}}\tilde{q}_z-\frac{5}{2}\tau. \tag{44}$$

In Eq. (44) Navier–Stokes law for shear-stress in dimensionless form was used, i.e.,

$$\tilde{\sigma}_{rz}^{\mathrm{NSF}} = -\,\mathrm{Kn}\frac{\partial \tilde{v}_z}{\partial \tilde{r}}. \tag{45}$$

Equation (44) is Fourier's law for axial heat conduction (applicable only for thermally driven flows),

$$\tilde{q}_z^{\mathrm{NSF}} = -\,\frac{5}{2}\frac{\mathrm{Kn}}{\mathrm{Pr}}\tau. \tag{46}$$

Since σ_{rz} is of $\mathcal{O}(\mathrm{Kn})$, it follows from Eq. (41a) and also from Eq. (44) that pressure gradient $\wp$ is first-order in terms of Knudsen number, $\mathcal{O}(\wp)=\mathcal{O}(\mathrm{Kn})$. Hence, $\wp$ in Eq. (41b) provides a second-order contribution to the axial heat flow, and as depicted in Eq. (44) it vanishes in the hydrodynamic limit.[24] The radial velocity distribution can be found by integrating Eq. (44). Depending on the kinetic model, the integrating constants must be evaluated from the linearized form of the approximate slip conditions [cf. Eqs. (34) or Eq. (35)] that read

$$\begin{aligned}\tilde{v}_z^{\mathrm{NSF\text{-}BE}} &= \frac{2-\chi}{\chi}\sqrt{\frac{\pi}{2}}\mathrm{Kn}\frac{\partial \tilde{v}_z}{\partial \tilde{r}}n_r + \frac{3}{4}\mathrm{Kn}\,\tau \\ &\quad -\frac{1}{6}\mathrm{Kn}^2\left(5\frac{\partial}{\partial \tilde{r}}+\frac{1}{\tilde{r}}\right)\frac{\partial \tilde{v}_z}{\partial \tilde{r}}, \\ \tilde{v}_z^{\mathrm{NSF\text{-}BGK}} &= \frac{2-\chi}{\chi}\sqrt{\frac{\pi}{2}}\mathrm{Kn}\frac{\partial \tilde{v}_z}{\partial \tilde{r}}n_r + \frac{1}{2}\mathrm{Kn}\,\tau - \mathrm{Kn}^2\frac{\partial^2 \tilde{v}_z}{\partial \tilde{r}^2}.\end{aligned} \tag{47}$$

In Eq. (47) both Navier–Stokes and Fourier laws in dimensionless form [Eqs. (45) and (46)] were used.

(ii) The temperature problem.

R13 case. Thermal behavior of the gas is governed by the equations

$$\left(\frac{\partial}{\partial \tilde{r}}+\frac{1}{\tilde{r}}\right)\tilde{q}_r = 0, \tag{48a}$$

$$\left(\frac{\partial}{\partial \tilde{r}}+\frac{1}{\tilde{r}}\right)\tilde{m}_{rzz} = -\frac{1}{\mathrm{Kn}}\tilde{\sigma}_{zz}, \tag{48b}$$

$$-\frac{4}{5}\frac{\tilde{q}_r}{\tilde{r}}+\frac{\partial \tilde{m}_{rrr}}{\partial \tilde{r}}+\frac{\tilde{m}_{rrr}-2\tilde{m}_{r\varphi\varphi}}{\tilde{r}} = -\frac{1}{\mathrm{Kn}}\tilde{\sigma}_{rr}, \tag{48c}$$

$$\begin{aligned}&\frac{\partial \tilde{\sigma}_{rr}}{\partial \tilde{r}}+\frac{2\tilde{\sigma}_{rr}+\tilde{\sigma}_{zz}}{\tilde{r}}+\frac{1}{2}\left(\frac{\partial \tilde{R}_{rr}}{\partial \tilde{r}}+\frac{2\tilde{R}_{rr}+\tilde{R}_{zz}}{\tilde{r}}\right)+\frac{1}{6}\frac{\partial \tilde{\Delta}}{\partial \tilde{r}} \\ &\quad = -\frac{\mathrm{Pr}}{\mathrm{Kn}}\tilde{q}_r - \frac{5}{2}\frac{\partial \tilde{\theta}}{\partial \tilde{r}},\end{aligned} \tag{48d}$$

with the constitutive relations

$$\begin{aligned}&\tilde{\Delta} = \tilde{R}_{zz} = 0, \quad \tilde{R}_{rr} = -\,B_2\,\mathrm{Kn}\frac{\tilde{q}_r}{\tilde{r}}, \\ &\tilde{m}_{rrr} = \frac{3}{5}C\,\mathrm{Kn}\left(\frac{\partial \tilde{\sigma}_{rr}}{\partial \tilde{r}}-\frac{2}{3}\frac{2\tilde{\sigma}_{rr}+\tilde{\sigma}_{zz}}{\tilde{r}}\right), \\ &\tilde{m}_{r\varphi\varphi} = C\,\mathrm{Kn}\left(-\frac{7}{15}\frac{\partial \tilde{\sigma}_{rr}}{\partial \tilde{r}}-\frac{1}{3}\frac{\partial \tilde{\sigma}_{zz}}{\partial \tilde{r}}+\frac{8}{15}\frac{2\tilde{\sigma}_{rr}+\tilde{\sigma}_{zz}}{\tilde{r}}\right), \\ &\tilde{m}_{rzz} = C\,\mathrm{Kn}\left(\frac{1}{3}\frac{\partial \tilde{\sigma}_{zz}}{\partial \tilde{r}}-\frac{2}{15}\frac{\partial \tilde{\sigma}_{rr}}{\partial \tilde{r}}-\frac{2}{15}\frac{2\tilde{\sigma}_{rr}+\tilde{\sigma}_{zz}}{\tilde{r}}\right),\end{aligned} \tag{49}$$

and the linearized boundary conditions

$$\tilde{q}_r = \frac{-\chi}{2-\chi}\sqrt{\frac{2}{\pi}}\left(2\tilde{\mathcal{T}}+\frac{1}{2}\tilde{\sigma}_{rr}+\frac{1}{15}\tilde{\Delta}+\frac{5}{28}\tilde{R}_{rr}\right)n_r, \tag{50a}$$

$$\tilde{m}_{rrr} = \frac{\chi}{2-\chi}\sqrt{\frac{2}{\pi}}\left(\frac{2}{5}\tilde{\mathcal{T}}-\frac{7}{5}\tilde{\sigma}_{rr}+\frac{1}{75}\tilde{\Delta}-\frac{1}{14}\tilde{R}_{rr}\right)n_r, \tag{50b}$$

$$\tilde{m}_{rzz} = \frac{-\chi}{2-\chi}\sqrt{\frac{2}{\pi}}\left(\frac{1}{5}\tilde{\mathcal{T}}+\frac{1}{14}\tilde{R}_{zz}+\tilde{\sigma}_{zz}-\frac{1}{5}\tilde{\sigma}_{rr}+\frac{1}{150}\tilde{\Delta}\right)n_r. \tag{50c}$$

Equation (48a) is the linearized energy balance in dimensionless form where the nonlinear viscous heating term is omitted, compare with Eq. (12). The other equations are linearized balance equations for normal components of the stress tensor and heat-flux vector.

Navier–Stokes–Fourier case. Fourier's law for the radial direction is given on the right-hand side of Eq. (48d), $\tilde{q}_r=-(5/2)(\mathrm{Kn}/\mathrm{Pr})\,\partial\tilde{\theta}/\partial\tilde{r}$. Substitution into Eq. (48a) gives an explicit equation for temperature,

$$\left(\frac{\partial}{\partial \tilde{r}}+\frac{1}{\tilde{r}}\right)\frac{\partial \tilde{\theta}}{\partial \tilde{r}} = 0. \tag{51}$$

Integrating the above equation introduces a constant which must be determined from the linearized temperature jump condition,

$$\begin{aligned}\tilde{\mathcal{T}}^{\mathrm{NSF\text{-}BE}} &= \frac{2-\chi}{\chi}\frac{15}{8}\sqrt{\frac{\pi}{2}}\mathrm{Kn}\frac{\partial \tilde{\theta}}{\partial \tilde{r}}n_r \\ &\quad -\frac{3}{14}\mathrm{Kn}^2\left(12\frac{\partial}{\partial \tilde{r}}+\frac{1}{\tilde{r}}\right)\frac{\partial \tilde{\theta}}{\partial \tilde{r}}, \\ \tilde{\mathcal{T}}^{\mathrm{NSF\text{-}BGK}} &= \frac{2-\chi}{\chi}\frac{5}{4}\sqrt{\frac{\pi}{2}}\mathrm{Kn}\frac{\partial \tilde{\theta}}{\partial \tilde{r}}n_r \\ &\quad -\frac{1}{4}\mathrm{Kn}^2\left(6\frac{\partial}{\partial \tilde{r}}-\frac{1}{\tilde{r}}\right)\frac{\partial \tilde{\theta}}{\partial \tilde{r}}.\end{aligned} \tag{52}$$

(iii) The density/pressure problem.

R13 case. Once the temperature problem is solved, we can integrate the linear form of the radial momentum balance [Eq. (10)],

$$\frac{\partial \tilde{p}}{\partial \tilde{r}} + \frac{\partial \tilde{\sigma}_{rr}}{\partial \tilde{r}} + \frac{2\tilde{\sigma}_{rr} + \tilde{\sigma}_{zz}}{\tilde{r}} = 0. \tag{53}$$

On account of Eq. (38) one can recast Eq. (53) as

$$\frac{\partial \tilde{\rho}}{\partial \tilde{r}} + \frac{\partial \tilde{\theta}}{\partial \tilde{r}} + \frac{\partial \tilde{\sigma}_{rr}}{\partial \tilde{r}} + \frac{2\tilde{\sigma}_{rr} + \tilde{\sigma}_{zz}}{\tilde{r}} = 0, \tag{54}$$

in order to find radial density deviations. Integrating the above equation introduces another integrating constant, which must be determined from the auxiliary condition (33), which in proper dimensionless form reads

$$\int_0^1 (\tilde{\rho} + 1)\tilde{r}d\tilde{r} = \text{const}. \tag{55}$$

Navier–Stokes–Fourier case. Based on the Navier–Stokes law the normal stress components, also known as non-Newtonian stresses, vanish in the hydrodynamic limit $\tilde{\sigma}_{rr}=\tilde{\sigma}_{zz}=0$. Then the density/pressure problem simplifies to $\tilde{\rho}+\tilde{\theta}=\text{const}$.

VII. SOLUTIONS

In this section, explicit linear solutions for Poiseuille and thermal transpiration flows in tubes are presented for the velocity problem. Although the temperature problem in Eqs. (48) and (49) is linear, due to the coupling between the non-Newtonian components of the stress tensor via the curvature terms, an explicit solution for it is not accessible. This restriction of obtaining analytical solution for the temperature problem is also reported in our discussion of cylindrical Couette flows.[15]

As in Ref. 15, the linear temperature problem can be solved numerically with basic finite difference methods, which yield $\tilde{q}_r=\tilde{\sigma}_{zz}=\tilde{\sigma}_{rr}=\tilde{\theta}=0$ for symmetric temperature distributions on the tube. Similarly, trivial solutions for density and pressure can be concluded from the temperature problem solution that are $\tilde{\rho}=\tilde{p}=0$. This trivial solution means that in the linear regime flow is isothermal. Nonzero solutions for $\{\tilde{q}_r, \tilde{\sigma}_{zz}, \tilde{\sigma}_{rr}, \tilde{\theta}, \tilde{\rho}, \tilde{p}\}$ can be obtained when a non-symmetric temperature distribution is defined on the tube wall, however, this is not a conventional setting for tube flows.

A. Poiseuille flow

In the Poiseuille flow where the process is driven by the pressure gradient $\wp$, the velocity problem [Eqs. (41) and (42)] reduces further to

$$\left(\frac{\partial}{\partial \tilde{r}} + \frac{1}{\tilde{r}}\right)\tilde{\sigma}_{rz} = -\wp, \tag{56a}$$

$$-\wp + \frac{B_2\,\text{Kn}}{4}\left(\frac{\partial}{\partial \tilde{r}} + \frac{1}{\tilde{r}}\right)\frac{\partial \tilde{q}_z}{\partial \tilde{r}} = -\frac{\text{Pr}}{\text{Kn}}\tilde{q}_z, \tag{56b}$$

$$\frac{2}{5}\frac{\partial \tilde{q}_z}{\partial \tilde{r}} = -\frac{1}{\text{Kn}}\tilde{\sigma}_{rz} - \frac{\partial \tilde{v}_z}{\partial \tilde{r}}. \tag{56c}$$

The solution for the above system follows by integration as

$$\tilde{\sigma}_{rz} = \underline{\frac{\mathsf{C}_1}{\tilde{r}} - \frac{\wp}{2}\tilde{r}}, \tag{57a}$$

$$\tilde{q}_z = \mathsf{C}_2\mathcal{J}_0\left(\frac{2}{\text{Kn}}\sqrt{\frac{\text{Pr}}{B_2}}\tilde{r}\right) + \mathsf{C}_3\mathcal{Y}_0\left(\frac{2}{\text{Kn}}\sqrt{\frac{\text{Pr}}{B_2}}\tilde{r}\right) + \frac{\text{Kn}}{\text{Pr}}\wp, \tag{57b}$$

$$\tilde{v}_z = \underline{\mathsf{C}_4 + \frac{\wp}{4\,\text{Kn}}\tilde{r}^2 - \frac{\mathsf{C}_1}{\text{Kn}}\ln(\tilde{r})} - \frac{2}{5}\tilde{q}_z. \tag{57c}$$

$\mathsf{C}_1-\mathsf{C}_4$ are the integrating constants, which need to be determined from the boundary conditions.

The underlined terms indicate the solution for the NSF equations. Note that both R13 and NSF systems yield the same solution for shear stress. The NSF system predicts heat flux only in the direction of the temperature gradient, thus, it cannot predict the axial heat flux $\tilde{q}_z$ in this isothermal flow. This streamwise heat flow, also known as mechanocaloric heat flux,[31,32] is not driven by temperature gradient, and is a pure rarefaction effect. The zeroth-order Bessel functions $\{\mathcal{J}_0, \mathcal{Y}_0\}$ in the mechanocaloric heat-flux describe Knudsen boundary layers, and $\text{Kn}\wp/\text{Pr}$ is a second-order bulk effect, as described in Sec. VI, $\mathcal{O}(\wp)=\mathcal{O}(\text{Kn})$. The term C_4 is the macroscopic slip velocity, while the microscopic slip velocity is $-2\tilde{q}_z/5$ (at $\tilde{r}=1$).

B. Transpiration flow

The thermal transpiration (creep) flow is induced by the axial temperature gradient τ, while $\wp=0$. Hence, the velocity problem in Eqs. (41) and (42) takes the form

$$\left(\frac{\partial}{\partial \tilde{r}} + \frac{1}{\tilde{r}}\right)\tilde{\sigma}_{rz} = 0, \tag{58a}$$

$$\frac{B_2\,\text{Kn}}{4}\left(\frac{\partial}{\partial \tilde{r}} + \frac{1}{\tilde{r}}\right)\frac{\partial \tilde{q}_z}{\partial \tilde{r}} = -\frac{\text{Pr}}{\text{Kn}}\tilde{q}_z - \frac{5}{2}\tau, \tag{58b}$$

$$\frac{2}{5}\frac{\partial \tilde{q}_z}{\partial \tilde{r}} = -\frac{1}{\text{Kn}}\tilde{\sigma}_{rz} - \frac{\partial \tilde{v}_z}{\partial \tilde{r}}. \tag{58c}$$

Integrating Eq. (58) gives the general solution as

$$\tilde{\sigma}_{rz} = \underline{\frac{\mathsf{C}_1}{\tilde{r}}}, \tag{59a}$$

$$\tilde{q}_z = \mathsf{C}_2 \mathcal{J}_0\left(\frac{2}{\mathrm{Kn}}\sqrt{\frac{\mathrm{Pr}}{B_2}}\tilde{r}\right) + \mathsf{C}_3 \mathcal{Y}_0\left(\frac{2}{\mathrm{Kn}}\sqrt{\frac{\mathrm{Pr}}{B_2}}\tilde{r}\right) \underline{- \frac{5\ \mathrm{Kn}}{2\ \mathrm{Pr}}\tau}, \tag{59b}$$

$$\tilde{v}_z = \underline{\mathsf{C}_4 - \frac{\mathsf{C}_1}{\mathrm{Kn}}\ln(\tilde{r}) - \frac{2}{5}\tilde{q}_z}, \tag{59c}$$

with the underlined terms as hydrodynamic solutions. Similar to Poiseuille flow, the stress solutions for NSF and R13 are identical. The axial heat flux is a superposition of Knudsen boundary layers $\{\mathcal{J}_0, \mathcal{Y}_0\}$ and a Fourier heat conduction that is forced by the axial temperature gradient τ. In the velocity solution, C_4 and the contribution of the Fourier's law represent the slip velocity (temperature-driven plug flow).

VIII. RESULTS AND DISCUSSION

This section provides comparison between our theoretical results and kinetic solutions for the Boltzmann equation. Radial distributions of stress, velocity, streamwise heat flux, and Knudsen layers are compared to available kinetic data. Moreover, for both Poiseuille and transpiration flows, the reduced mass flow rate, M, and the reduced thermal energy flow rate, E, are compared to Boltzmann data. The mass and thermal energy flow rates are defined as[16,33,34]

$$M = 2\sqrt{2}\int_0^1 |\tilde{v}_z|\tilde{r}d\tilde{r}, \quad E = 2\sqrt{2}\int_0^1 |\tilde{q}_z|\tilde{r}d\tilde{r}, \tag{60}$$

where the factor $2\sqrt{2}$ is included to match dimensionless definitions of M and E in the kinetic simulations. The influence of gas rarefaction, kinetic model, and boundary accommodation coefficients will be investigated on mass and energy transport in the axial direction.

Based on the applied kinetic model, we categorize the available kinetic data in two groups, namely, the linearized Boltzmann equation (BE) data and Bhatnagar–Gross–Krook (BGK) data. In each category different numerical schemes are utilized,[16] but the main difference between the BE and BGK models is the value of the Prandtl number Pr, where the BGK model fails to predict the correct Prandtl number. In comparisons of our solutions with kinetic data we use the coefficients given in Eqs. (27) and (28) as approximates for the BE and BGK models. Our general solutions in Eqs. (57b) and (59b) explicitly show that Pr and B_2 affect the thickness of Knudsen layers and bulk values. This observation is one of the advantages of analytical approach, which is not easily achievable in kinetic solutions.

Conventionally, in kinetic approaches a rarefaction parameter δ is defined as[16]

$$\delta = \frac{\sqrt{\pi}}{2}\frac{\mathcal{L}}{\lambda_0}, \tag{61}$$

where $\mathcal{L}$ and λ_0 are reference length scale (here, the radius of the tube R) and mean free path in the local equilibrium state, respectively. The kinetic theory of gases gives the mean free path with respect to macroscopic quantities as[35]

$$\lambda_0 = \sqrt{\frac{\pi\theta_0}{2}}\frac{\mu_0}{p_0}. \tag{62}$$

Replacement of λ_0 from Eq. (62) into Eq. (61) and then comparison with Eq. (40) gives a relation between Knudsen number and rarefaction parameter

$$\mathrm{Kn} = \frac{1}{\sqrt{2}\delta}, \tag{63}$$

which has been used to relate our solutions to the kinetic data.

A. Poiseuille flow

The solution for Poiseuille flow is given in Eq. (57), where for the sake of compatibility with the Boltzmann data we shall set $\wp = 1$. Since the solutions must be finite at $\tilde{r}=0$, then $\mathsf{C}_1 = \mathsf{C}_3 = 0$. The only unknown constant in the Navier–Stokes–Fourier solution is C_4 which can be evaluated from the linearized slip condition (47) at $\tilde{r}=1$. For the R13 solution the constants $\{\mathsf{C}_2, \mathsf{C}_4\}$ follow from the boundary conditions (43a) and (43b). Expressions for these constants are presented in Appendix B. Since $\mathsf{C}_1 = 0$, shear stress in NSF and R13 linearly depends on radial position, and its magnitude is proportional to the constant pressure gradient (or force), i.e., $\tilde{\sigma}_{rz} = -\wp\tilde{r}/2$.

In Fig. 2 the radial distribution of velocity and mechanocaloric heat flux are shown for $\chi = 1$ and $\mathrm{Kn} = \{0.07, 0.14, 0.35\}$, corresponding to $\delta = \{10, 5, 2\}$. For proper scaling the kinetic data are multiplied with the factor $\sqrt{2}/\delta$. Plots (a) and (b) compare the velocity solutions with both BGK and linear Boltzmann equation (BE) data, respectively. In Poiseuille flow the solutions for BGK and BE are very close. As shown in plot (b), for the small Knudsen number $\mathrm{Kn} = 0.07$, all models show fair agreement with the kinetic solution. As the Knudsen number increases the Navier–Stokes–Fourier equations with first-order slip condition yield unsatisfactory bulk solution, however, it provides a better approximation of the slip velocity. By predicting a larger slip, the second-order slip condition shifts the NSF solution toward the R13 and kinetic results. Compared to NSF with second-order slip condition, R13 shows better agreement with kinetic data near the wall. This improvement is the effect of third-order boundary conditions and Knudsen boundary layer.

In the velocity profile for $\mathrm{Kn} = 0.35$, R13 shows maximum error at $r=0$ and $r/R=1$. In plot (b) these errors are 10% and 22% at the center of tubes and on the wall, respectively. These errors are calculated as (data−R13)/R13.

In plot (c), the mechanocaloric heat flux (Knudsen layer) in Poiseuille flow is compared to BE data (BGK data are not available for this case). This high-order nonequilibrium heat

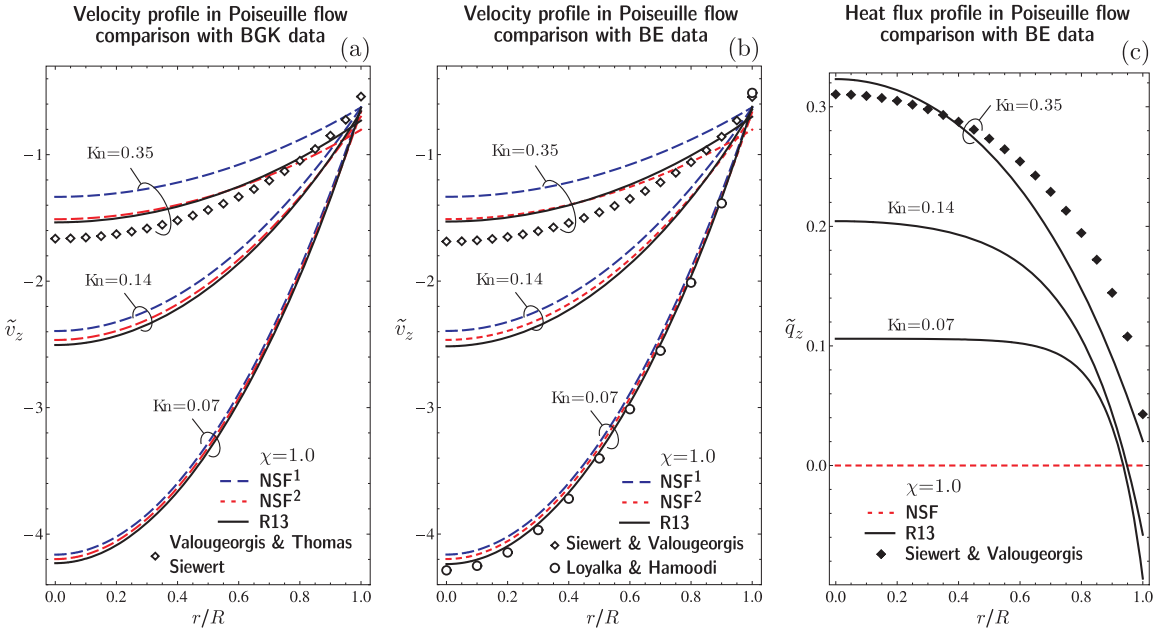

FIG. 2. (Color online) Radial distribution of velocity and mechanocaloric heat flux (Knudsen layer) in Poiseuille flow for Kn={0.07,0.14,0.35} and fully diffusive tube surface, χ=1. Results from Navier–Stokes–Fourier with first-order slip condition (NSF^1; long-dashed blue line), Navier–Stokes–Fourier with second-order slip condition (NSF^2; dotted red line), and regularized 13-moment with third-order boundary conditions (R13; solid black line) are compared to kinetic data (symbols). The BGK data are taken from Refs. 33 and 34 and BE data are from Refs. 36 and 37.

flow, which points in opposite direction to mass flow and is not driven by temperature gradient, cannot be predicted by NSF. As depicted, for small Knudsen numbers, a two-way heat flow occurs; streamwise in a narrow layer near the wall and counter-stream elsewhere. This phenomenon is also observed in Poiseuille flow in parallel-plate microchannels.[12]

Figure 3 shows the reduced mass flow rate in Poiseuille flow M_P for fully diffusive walls χ=1 in the hydrodynamic regime. It shows that for small Knudsen numbers both NSF and R13 agree with kinetic data, taken from Ref. 38. Indeed, the agreement between velocity profiles (cf. Fig. 2) is the reason for the precise prediction of mass flow rate. The kinetic data in Fig. 3 are obtained based on the BGK model,

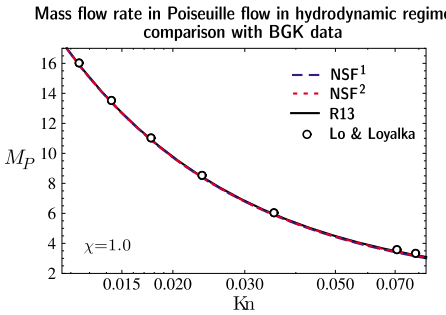

FIG. 3. (Color online) The reduced mass flow rate in Poiseuille flow obtained from Navier–Stokes–Fourier with first-order slip condition (NSF^1; long-dashed blue line), Navier–Stokes–Fourier with second-order slip condition (NSF^2; dotted red line), and regularized 13-moment with third-order boundary conditions (R13; solid black line) are compared to BGK kinetic data (symbols) from Ref. 38. The comparison is presented for small Knudsen numbers and fully diffusive tube surface, χ=1. The comparison confirms that in the slip flow regime where Kn$<$0.1, the results are very close.

hence we used coefficients in Eq. (28) to evaluate our results. Similar BGK data were also reported earlier by Cercignani and Sernagiotto.[17]

Kinetic solutions for Poiseuille flow in the transition regime confirm Knudsen's experimental observation,[19] that in low pressure Poiseuille flows the mass flow rate as a function of Knudsen number exhibits a minimum. This phenomenon, which is known as Knudsen minimum paradox, is observed in both parallel-plate channel and tube flows.[1]

Figure 4 shows the variations of mass flow rate in Poiseuille flow with respect to Knudsen number and accommodation coefficient of the tube surface. Unlike Fig. 3, which is restricted to the hydrodynamic regime, here the Knudsen number varies across the transition regime. NSF solutions with first- and second-order slip conditions are shown in plots (a)–(d), while R13 results are given in plots (e) and (f). Additionally, we compared our solutions with both BGK (left plots) and BE (right plots) data. The symbols present kinetic data for different accommodation coefficients χ ={0.6,0.8,1.0}. Small values for χ represent smooth walls with less friction that result in larger flow rates. The results in Fig. 4 show that for small values of χ the validity of macroscopic models is extended to larger values for Kn. Here, we compare the accuracy of NSF and R13 with kinetic data for χ=1, which is commonly assumed in engineering applications. NSF with first-order slip condition in plots (a) and (b) does not exhibit any minimum and is acceptable only for very small Knudsen numbers, Kn$<$0.1. The second-order slip condition extends the validity of the NSF system up to Kn$\lesssim$0.6 and enables the NSF system to capture a minimum. The R13 solution [cf. plots (e) and (f)] provide acceptable approximation of the flow rate in the transition

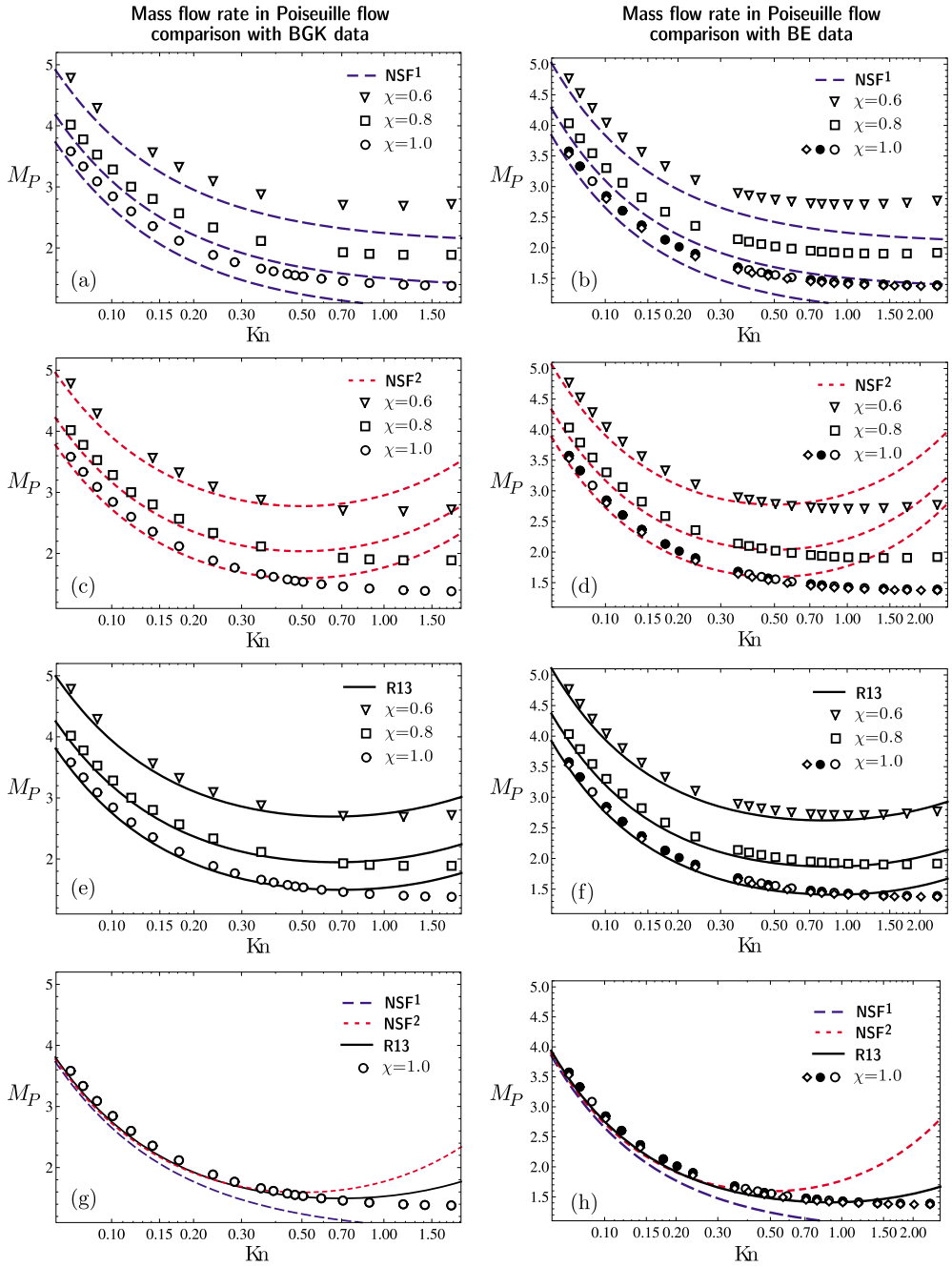

FIG. 4. (Color online) The effects of Knudsen number and surface accommodation on the reduced mass flow rate in Poiseuille flow in transition flow regime. Navier–Stokes–Fourier with first-order slip condition (NSF[1]; long-dashed blue line), Navier–Stokes–Fourier with second-order slip condition (NSF[2]; dashed red line), and regularized 13-moment with third-order boundary conditions (R13; solid black line) are compared to kinetic data (symbols) for $\chi=\{0.6,0.8,1.0\}$. Left and right plots correspond to BGK and BE solutions, respectively. BGK data for $\chi=1$ shown by circles are from Ref. 38, while triangles and cubes are taken from Refs. 39 and 40. The BE data for $\chi=1$ shown by black circles and diamonds are from Refs. 36 and 37, respectively. All other data are from Ref. 25. It is shown that second-order slip condition improves the NSF solution in transition flow regime. In plots (g) and (h) all solutions for $\chi=1$ are compared.

regime; they are valid for $\mathrm{Kn}<1.0$ in the BGK model and $\mathrm{Kn}<1.7$ in the BE model. Our criterion to set these range for Knudsen number is $(\text{data}-\text{model})/\text{model}\lesssim 7\%$, since in engineering applications (depending on the application) $\sim 10\%$ error is generally recognized as a reasonable error margin.

For better comparison, the results for fully diffusive walls are compared in plots (g) and (h). For $\chi=1$ the kinetic solution gives the minimum around $\mathrm{Kn}=2.0$, while as our best candidate, R13, predicts this minimum around $\mathrm{Kn}=0.7$ and $\mathrm{Kn}=1.0$ for BGK and BE models.

We emphasize that for proper comparison with the kinetic data our results in Fig. 4 are obtained separately with BGK model coefficients (28) and linearized Boltzmann model coefficients (27). The reduced thermal energy flow rate in Poiseuille flow, E_P, is discussed in Sec. VIII C.

B. Transpiration flow

The solution for thermal transpiration/creep problem is given in Eq. (59), where for the sake of compatibility with

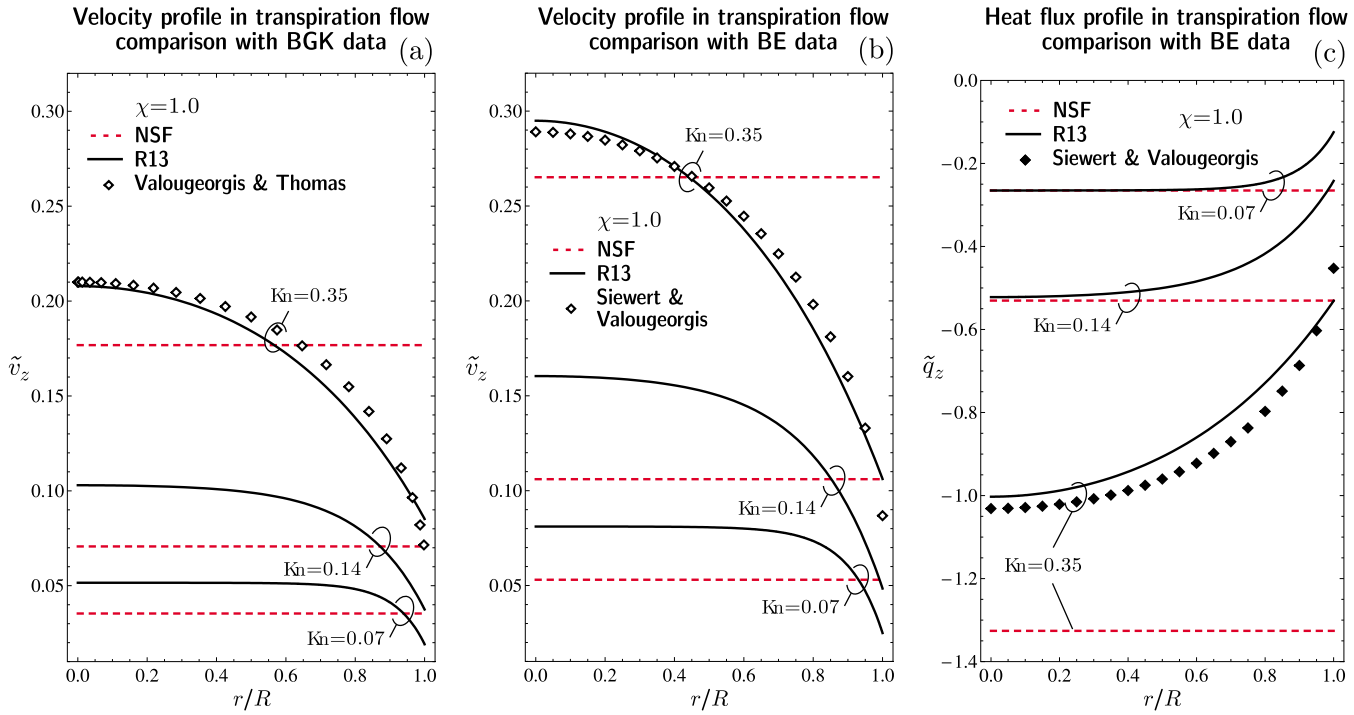

FIG. 5. (Color online) Radial distribution of velocity and heat flux in transpiration flow for Kn={0.07,0.14,0.35} and fully diffusive tube surface, $\chi=1$. Results from Navier–Stokes–Fourier (NSF; dotted red line) and regularized 13-moment (R13; solid black line) are compared to kinetic data (symbols). The BGK data are taken from Refs. 33 and 34 and BE data are from Refs. 36 and 37. Note that for both velocity and heat flux NSF yields constant solutions. In transpiration flow the first- and second-order slip conditions for NSF are equivalent.

the kinetic data we set $\tau=1$. Since these solutions are finite at $\tilde{r}=0$, then $\mathsf{C}_1=\mathsf{C}_3=0$. The constant C_4 for the NSF system can be evaluated from the linearized slip condition in Eq. (47) at $\tilde{r}=1$. For the R13 solution the constants $\{\mathsf{C}_2,\mathsf{C}_4\}$ require boundary conditions (43a) and (43b). Expressions for these constants are presented in Appendix B.

With $\mathsf{C}_1=0$ the shear stress for both NSF and R13 systems vanishes, $\tilde{\sigma}_{rz}=0$. Accordingly, for thermal transpiration flow, the slip conditions (34) and (35) in dimensionless form reduce to

$$\tilde{v}_z^{\text{NSF-BE}}=\frac{3}{4}\text{Kn}\ \tau,\quad \tilde{v}_z^{\text{NSF-BGK}}=\frac{1}{2}\text{Kn}\ \tau,$$

that means in the linear limit the second-order slip condition degrades to a first-order condition. Due to this simplification, the effects of accommodation coefficients do not appear in the slip condition for hydrodynamics.

In Fig. 5 profiles of velocity and heat flux in transpiration flow are shown for $\chi=1$ and Kn={0.07,0.14,0.35}, which correspond to $\delta=\{10,5,2\}$. Plots (a) and (b) compare the velocity solutions with BGK and linear Boltzmann equation (BE) data, respectively. For proper scaling the kinetic data are multiplied with the factor $\sqrt{2}/\delta$. As depicted, unlike the Poiseuille flow, in transpiration flow the solutions for BGK and BE models are quite different. Our analytical solution shows that this inconsistency roots in the different values for Pr and the coefficient B_2. The results confirm that the magnitude of mass and heat flows increases with the rarefaction degree. Navier–Stokes–Fourier yields a plug flow across the tube cross section and drastically overestimates the mass and heat fluxes near the wall. In plot (c), the axial heat flux in transpiration flow is compared to BE data. This heat flow is a superposition of Fourier heat flow, i.e., the NSF solution, and the mechanocaloric heat flow [see Eq. (59b)]. The mechanocaloric heat flow (Knudsen layer), which occurs in mass flow direction competes with the constant Fourier heat flow, and helps the R13 solution to match the kinetic results. For small Knudsen numbers, where the effects of Knudsen boundary layers are limited to the wall neighborhood, NSF and R13 predict the same heat flux at the center of the pipe.

For Kn=0.35 the R13 solution for velocity shows 18% error with respect to kinetic data at $r/R=1$. For the heat flux solution the error is around 14% at $r/R=1$ and 7% at $r/R=0.65$. These errors are calculated as (data−R13)/R13.

Figure 6 shows the variations of the reduced mass and energy flow rates in thermal transpiration flow with respect to Knudsen number and surface accommodation coefficient. Our analytical results are compared to BGK and BE kinetic data for moderately rarefied flows in the transition regime. The BGK data in plots (a) and (c) are taken from Ref. 41. BGK data for $\chi=1$ are also available in Ref. 33. The BE data in plots (b) and (d) are from Refs. 25 and 36. Plots (a) and (b) show that for Kn<0.3 the mass flow rate is a weak function of accommodation coefficients. However, for larger Knudsen numbers the effects of the accommodation coefficient become significant. Linearized NSF provides a rough approximation of the kinetic data for Kn$\lesssim$0.2. Nevertheless, it neglects the effects of surface accommodation and drastically overestimates the mass transfer when surface effects come into account, i.e., for Kn>0.3. The R13 system, on the other hand, yields remarkable agreement with kinetic data up

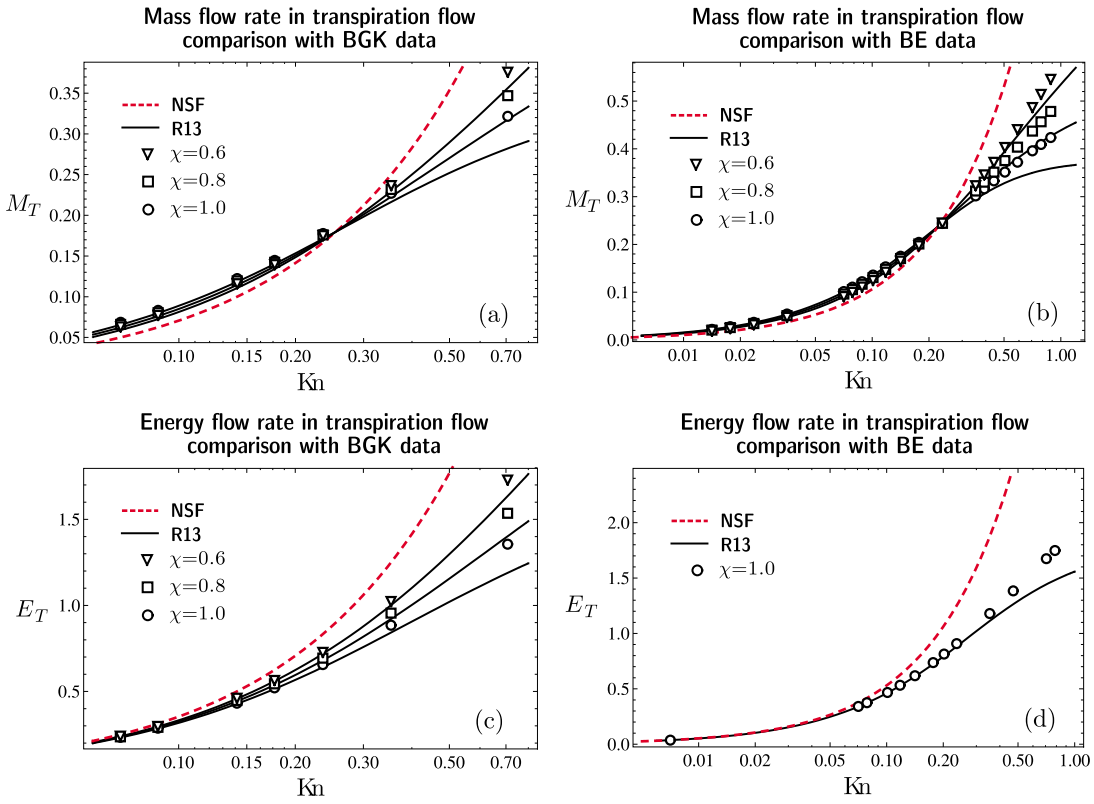

FIG. 6. (Color online) The effects of Knudsen number and surface accommodation on the reduced mass and thermal energy flow rates in transpiration flow in the transition regime. Results from Navier–Stokes–Fourier (NSF; dotted red line) and regularized 13-moment (R13; solid black line) are compared to kinetic data (symbols) for $\chi=\{0.6,0.8,1.0\}$. Plots (a) and (c) present comparisons with BGK kinetic data taken from Ref. 41. In plot (b) and (d) our solutions are compared to BE kinetic data from Refs. 25 and 36, respectively. In transpiration flow the first- and second-order slip conditions for NSF are equal and fail to capture the influence of the accommodation coefficient.

to Kn=0.5. The boundary conditions (43a) and (43b) allow the R13 system to take account for the surface effects. For small values of χ this agreement extends to Kn=0.7 for the BGK model, and Kn=1.0 for the BE model. Similar to Fig. 4, our criterion to set these range for Knudsen number is (data−model)/model$\lesssim$7%.

Plots (c) and (d) in Fig. 6 show the reduced thermal energy flow rate in transpiration flow. The Navier–Stokes–Fourier system, which only considers Fourier heat flow due to the axial temperature gradient, overestimates the energy flow above Kn=0.1, and fails to capture the surface effects. Similar to the reduced mass flow rate, R13 results are accurate for moderate Knudsen numbers. To the authors' knowledge, there are no linearized Boltzmann kinetic data available for reflective-diffusive surfaces ($\chi<1$).

C. Validity of Onsager's reciprocity relation

The well-known phenomenological laws of nonequilibrium thermodynamics are derived from the Onsager's theorem which relates thermodynamics forces to thermodynamics fluxes. Despite the independency of thermodynamics forces, they might cause several fluxes, i.e., cross effects.[42] An example for this is coexistence of both mass and energy fluxes due to pressure (or temperature) gradient in Poiseuille (or transpiration) flow, where the pressure (temperature) gradient is considered as the driving thermodynamic force.

For steady state flows in the linear regime the Onsager reciprocity relation can be derived[43,44] as

$$E_P = M_T. \tag{64}$$

Thus, energy flux driven by pressure force should be equal to the mass flux which is driven by temperature force (note that these quantities are defined in dimensionless form).

In Fig. 7 our theoretical results for the reduced thermal energy flow rate in Poiseuille flow E_P and the reduced mass flow rate in transpiration flow M_T are compared to kinetic data from Refs. 25 and 36. In the kinetic simulations Eq. (64) is valid for the entire range of Knudsen numbers and is usually used to validate the accuracy of computations. As shown, in the absence of a longitudinal temperature gradient, NSF fails to predict the mechanocaloric energy flux in Poiseuille flow, hence, the Onsager reciprocity relation is valid for the NSF system only when Kn$\to$0. On the other hand, R13 gives partial agreement, which extends up to Kn$\lesssim$0.25, with approximately 7% deviation.

D. Two-way Poiseuille and transpiration flows

In the case of simultaneous Poiseuille and transpiration flows, it is straightforward to show that a superposition of Poiseuille and transpiration solutions satisfies the general velocity problem [Eqs. (41a) to (43b)]. Accordingly, the general solution for the velocity reads

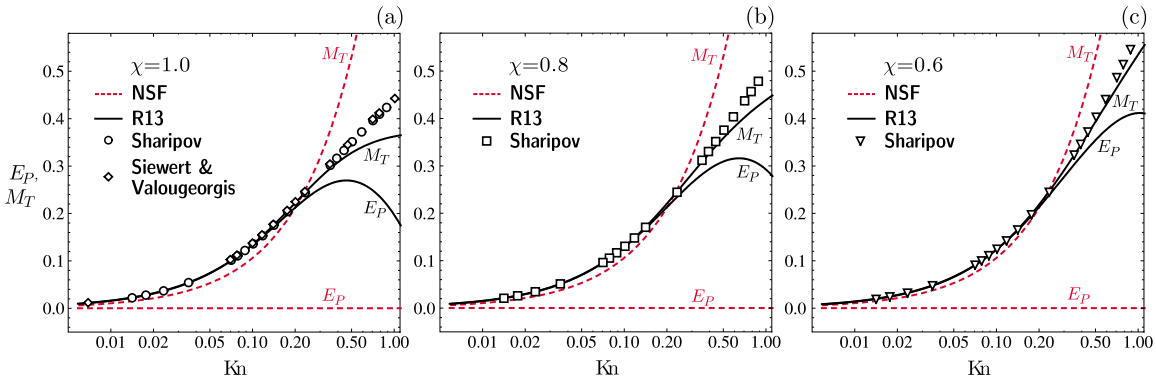

FIG. 7. (Color online) Validity of Onsager's reciprocity relation, $E_p=M_T$, is examined for Navier–Stokes–Fourier (NSF; dotted red lines) and regularized 13-moment (R13; solid black lines) equations. Our solutions for $\chi=\{1.0,0.8,0.6\}$ over moderate Knudsen numbers are compared to BE kinetic data (symbols) from Refs. 25 and 36. It is evident that in NSF system the Onsager's condition holds only for very small Knudsen numbers. However, R13 yields Onsager symmetry for $\mathrm{Kn}<0.2$.

$$\tilde{v}_z = \mathsf{C}_4 + \frac{\wp}{4\ \mathrm{Kn}} r^2 - \frac{2}{5}\left[\mathsf{C}_2 \mathcal{J}_0\left(\frac{2}{\mathrm{Kn}}\sqrt{\frac{\mathrm{Pr}}{B_2}}\tilde{r}\right) + \frac{\mathrm{Kn}}{\mathrm{Pr}}\wp - \frac{5\ \mathrm{Kn}}{2\ \mathrm{Pr}}\tau\right], \tag{65}$$

where, again, $\{\mathsf{C}_1,\mathsf{C}_3\}=0$, and $\{\mathsf{C}_2,\mathsf{C}_4\}$ are superpositions of the corresponding integrating constants for Poiseuille and transpiration flows, see Appendix B. In steady state condition, the net mass flow rate is zero,

$$\int_0^1 \tilde{v}_z \tilde{r} d\tilde{r} = 0. \tag{66}$$

Substituting the velocity solution (65) into condition (66) and then integrating, gives a relation between $\wp$, τ, and Kn, which reads

$$\tau = \wp\left(\frac{2}{5} - \frac{\mathrm{Pr}}{8\ \mathrm{Kn}^2}\right) + \frac{2}{5}\sqrt{\mathrm{Pr}\ B_2}\mathsf{C}_2 \mathcal{J}_1\left(\frac{2}{\mathrm{Kn}}\sqrt{\frac{\mathrm{Pr}}{B_2}}\right) - \frac{\mathrm{Pr}\ \mathsf{C}_4}{\mathrm{Kn}}. \tag{67}$$

Since the BGK model yields incorrect Prandtl number, it is erroneous in describing isothermal and nonisothermal flows simultaneously.[25] Thus, in this section we use BE coefficients (27) in our calculations, which correspond to the correct Prandtl number.

Figure 8 shows velocity profiles in simultaneous Poiseuille and transpiration flows for fully diffusive walls, $\chi=1$. As illustrated, a two-way flow is formed in the tube, in which the pressure-driven flow is dominant in the center of the tube and close to the wall thermal creep occurs in the opposite direction. In plot (a) the dimensionless pressure gradient is $\wp=0.1$, while the values for Knudsen number are $\mathrm{Kn}=\{0.1,0.15,0.2\}$, which correspond to $\tau=\{2.05,1.19,0.86\}$ according to Eq. (67). For a constant pressure gradient, when the Knudsen number increases, the required temperature gradient to satisfy condition (66) decreases. In plot (b), the Knudsen number is constant, $\mathrm{Kn}=0.1$, and different pressure gradients are chosen $\wp=\{0.1,0.3,0.5\}$, which yield $\tau=\{2.05,6.15,10.25\}$. Indeed, for a given set of $\{\mathrm{Kn},\mathrm{Pr},\chi,B_2\}$, Eq. (67) gives a linear relation between $\wp$ and τ.

E. Thermomolecular pressure difference

By replacing the integrating constants $\{\mathsf{C}_2,\mathsf{C}_4\}$ into Eq. (65) and integrating as in Eq. (66), the net mass flow rate splits as

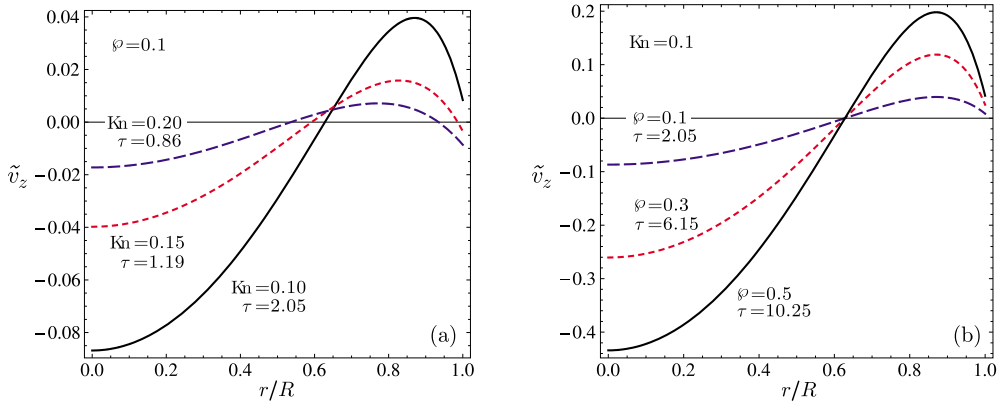

FIG. 8. (Color online) Two-way velocity fields in simultaneous Poiseuille and transpiration flows, where pressure-driven flow occurs in the middle of the tube, and temperature-driven flow close to the boundary. The flows have opposite directions, such that the net flow rate is zero. In plot (a) the pressure gradient is constant and the effects of Knudsen number variation are shown. In plot (b) the Knudsen number is fixed and different pressure gradients are examined. Both plots are shown for fully diffusive walls, $\chi=1$.

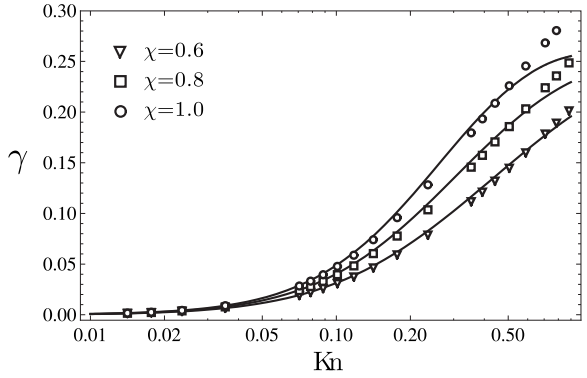

FIG. 9. The exponent of thermomolecular pressure difference γ, obtained from R13 equations for different accommodation coefficients, is compared to kinetic data (symbols) from Ref. 25.

$$M_{\text{net}} = \tau M_T - \wp M_P = 0. \tag{68}$$

Substitution of τ and $\wp$ from Eqs. (7) and (8) yields a simple expression for the exponent of thermomolecular pressure difference γ [cf. Eq. (1)],

$$\gamma = \frac{M_T}{M_P}. \tag{69}$$

In Fig. 9, values for γ obtained from our linear approach are compared to linear kinetic data.[25] Similar to our previous calculations for mass and energy flow rates, we observe consistency between our model and kinetic data for $\text{Kn} < 0.5$. For small accommodation coefficients this consistency extends to $\text{Kn} < 1.0$.

IX. CONCLUSION

A compact analytical model to describe moderately rarefied gas flows through long tubes caused by small pressure and temperature gradients has been presented. The model is based on the regularized 13-moment system, which from the previous studies[12–15,45] is realized as the smallest set of moment equations capable of approximating a rather rich array of rarefaction effects.

In the present work, dominant rarefaction effects in slow rarefied gas flows, i.e., Knudsen boundary layers, and their influence on mass and energy transfer along the tube, are described by the linearized R13 equations at very modest computational expense. The coefficients which describe Poiseuille flow, thermal transpiration flow, and their combination are calculated and compared to corresponding kinetic data. We included linear Navier–Stokes–Fourier results in our comparisons to emphasize their imperfection in describing rarefied gas flows.

Our calculations show that in contrast with classical hydrodynamics, the R13 equations successfully capture the mechanocaloric heat flow (Knudsen boundary layers) in both Poiseuille and thermal transpiration flows. This non-Fourier heat flow, which is not driven by temperature gradient, occurs near the tube walls. Although the amplitude of the mechanocaloric heat flow is small, it occupies a considerable portion of the cross section, therefore, it has a great impact on mass and energy flow rates. The Navier–Stokes–Fourier system fails to describe these nonequilibrium effects, however, the proposed second-order boundary conditions allow partial compensation for the missing rarefaction effects.

Furthermore, motivated by kinetic simulations, we examined our model subject to simultaneous Poiseuille and transpiration flows, which allows to investigate Onsager's reciprocity relation, two-way flow patterns, and thermomolecular pressure difference. Comparisons showed that the R13 equations yield satisfactory agreement with Boltzmann data in the early transition flow regime. Satisfaction of Onsager's relation is proposed as a new criterion to determine the range of validity of macroscopic transport equations (in terms of Knudsen number). It is shown that, according to Onsager's reciprocity relation, linearized R13 equations are applicable for flows in which $\text{Kn} \leq 0.25$.

To conclude, we must highlight the insufficiency of regularized 13-moment equations for highly rarefied flows, in which the magnitude of rarefaction effects is beyond the resolution of R13 equations. In such conditions, larger systems of moment equations are required.[46]

ACKNOWLEDGMENTS

This research was supported by the Natural Sciences and Engineering Research Council (NSERC).

APPENDIX A: SECOND-ORDER SLIP AND JUMP CONDITIONS FOR AXIAL FLOW IN TUBES

Explicit expressions for slip velocity $\mathcal{V}_z = v_z - v_z^W$ and temperature jump $\mathcal{T} = \theta - \theta_W$ can be obtained form the R13 boundary conditions (31a) and (31c) as

$$\mathcal{V}_z = \underline{-\frac{2-\chi}{\chi}\sqrt{\frac{\pi\theta}{2}}\frac{\sigma_{rz}}{\mathcal{P}}n_r - \frac{1}{5}\frac{q_z}{\mathcal{P}}} - \frac{1}{2}\frac{m_{rrz}}{\mathcal{P}} \tag{A1}$$

and

$$\mathcal{T} = \underline{-\frac{2-\chi}{\chi}\sqrt{\frac{\pi\theta}{2}}\frac{q_r}{2\mathcal{P}}n_r} + \frac{1}{4}\mathcal{V}^2 - \frac{1}{4}\frac{\theta\sigma_{rr}}{\mathcal{P}} - \frac{1}{30}\frac{\Delta}{\mathcal{P}} - \frac{5}{56}\frac{R_{rr}}{\mathcal{P}}. \tag{A2}$$

The above boundary conditions are of third-order, $\mathcal{O}(\text{Kn}^3)$. The underlined terms correspond to the well-known first-order slip velocity and temperature jump conditions,[28] where σ_{rz} and q_r require the NSF relations, i.e., Eqs. (29) and (30), and $\mathcal{P}^{\text{NSF}} = p$. We emphasize that in thermal-creep flow q_z in Eq. (A1) has a first-order contribution postulated by Fourier's law, but in Poiseuille flow q_z only represents second-order corrections. The additional terms in Eqs. (A1) and (A2) are higher-order moments which vanish in the NSF theory. However, their second-order contributions can be used to provide second-order corrections for the slip and jump conditions. To do so, we use a scaling approach based on the Chapman–Enskog expansion as in Ref. 9.

Density, temperature and velocity are equilibrium quantities and are not expanded, since they are of zeroth-order. The radial heat flux and shear stress are first-order quantities

$$q_r = \mathrm{Kn}\, \overset{*}{q}_r, \quad \sigma_{rz} = \mathrm{Kn}\, \overset{*}{\sigma}_{rz}, \tag{A3}$$

while second-order quantities are

$$q_z = \mathrm{Kn}^{\alpha}\, \overset{*}{q}_z, \quad \sigma_{rr} = \mathrm{Kn}^2\, \overset{*}{\sigma}_{rr}, \quad \sigma_{zz} = \mathrm{Kn}^2\, \overset{*}{\sigma}_{zz}, \quad \Delta = \mathrm{Kn}^2\, \overset{*}{\Delta},$$

$$R_{rr} = \mathrm{Kn}^2\, \overset{*}{R}_{rr}, \quad R_{zz} = \mathrm{Kn}^2\, \overset{*}{R}_{zz}, \quad m_{rrz} = \mathrm{Kn}^2\, \overset{*}{m}_{rrz}, \tag{A4}$$

$$m_{\varphi\varphi z} = \mathrm{Kn}^2\, \overset{*}{m}_{\varphi\varphi z}.$$

Note that the axial heat flux is of first-order in transpiration flow ($\alpha=1$), and second-order for Poiseuille flow ($\alpha=2$). The remaining quantities, which promote the R13 boundary conditions to be of third-order, are

$$R_{rz} = \mathrm{Kn}^3\, \overset{*}{R}_{rz}, \quad m_{rrr} = \mathrm{Kn}^3\, \overset{*}{m}_{rrr},$$

$$m_{r\varphi\varphi} = \mathrm{Kn}^3\, \overset{*}{m}_{r\varphi\varphi}, \quad m_{rzz} = \mathrm{Kn}^3\, \overset{*}{m}_{rzz}. \tag{A5}$$

The moments in (A3)–(A5) are scaled as $\mathcal{M} = \mathrm{Kn}^{\alpha}\, \overset{*}{\mathcal{M}}$, where the rescaled moment $\overset{*}{\mathcal{M}}$ is of order unity and α is the order of the moment $\mathcal{M}$.

Replacement of the scaled moments into the extended balance Eqs. (16)–(26) allows to identify their second-order terms. Accordingly, normal heat flux and shear stress balance reduce to the Fourier and Navier–Stokes laws,

$$\overset{*}{q}_r = -\frac{5\mu}{2\,\mathrm{Pr}}\frac{\partial\theta}{\partial r}, \quad \overset{*}{\sigma}_{rz} = -\mu\frac{\partial v_z}{\partial r}, \tag{A6}$$

and the required second-order moments read

$$\overset{*}{q}_z = \frac{7}{5}\left(1+\frac{1}{\mathrm{Pr}}\right)\frac{\overset{*}{\sigma}_{rz}\overset{*}{q}_r}{p} - \frac{\mu}{\rho\,\mathrm{Pr}}\left(\frac{\partial\overset{*}{\sigma}_{rz}}{\partial r} + \frac{\overset{*}{\sigma}_{rz}}{r}\right), \tag{A7}$$

$$\overset{*}{\sigma}_{rr} = \frac{4}{5}\frac{\mu}{p}\frac{\overset{*}{q}_r}{r} - \frac{6}{5}\frac{\overset{*2}{\sigma}_{rz}}{p}, \tag{A8}$$

$$\overset{*}{\sigma}_{zz} = \frac{8}{5}\frac{\overset{*2}{\sigma}_{rz}}{p}, \tag{A9}$$

$$\overset{*}{\Delta} = \frac{A_2\mu}{\rho}\left(\frac{\partial\overset{*}{q}_r}{\partial r} + \frac{\overset{*}{q}_r}{r}\right) - \frac{7\,\mathrm{Pr}\,A_2}{5}\frac{\overset{*2}{q}_r}{p} - (A_2 - 2A_1)\frac{\overset{*2}{\sigma}_{rz}}{\rho}, \tag{A10}$$

$$\overset{*}{R}_{rr} = \frac{B_2}{3}\frac{\mu}{\rho}\left(2\frac{\partial\overset{*}{q}_r}{\partial r} - \frac{\overset{*}{q}_r}{r}\right) - \frac{8\,\mathrm{Pr}\,B_2}{15}\frac{\overset{*2}{q}_r}{p} - \left(\frac{5B_2}{21} - \frac{B_1}{3}\right)\frac{\overset{*2}{\sigma}_{rz}}{\rho}, \tag{A11}$$

$$\overset{*}{m}_{rrz} = \frac{2C}{15}\frac{\mu}{\rho}\left(4\frac{\partial\overset{*}{\sigma}_{rz}}{\partial r} - \frac{\overset{*}{\sigma}_{rz}}{r}\right) - \frac{16C(1+\mathrm{Pr})}{75}\frac{\overset{*}{\sigma}_{rz}\overset{*}{q}_r}{p}. \tag{A12}$$

To obtain second-order corrections to slip and jump conditions, the third-order corrections in Eq. (A5) are dropped.

Subsequent substitution of Eqs. (A7)–(A12) into Eq. (A4) and then into Eqs. (A1) and (A2) gives the second-order slip and jump conditions, as presented in Eqs. (34)–(37). The last step includes replacement of Eq. (A6) into the obtained boundary conditions.

APPENDIX B: INTEGRATING CONSTANTS

For Poiseuille flow, the first- and second-order integrating constants for Navier–Stokes–Fourier solutions [cf. Eq. (57c)] can be obtained from their corresponding slip conditions, which give

$$\mathrm{C}_4^{\mathrm{NSF}^1} = -\wp\frac{\beta + \sqrt{2\pi}\,\mathrm{Kn}}{4\beta\,\mathrm{Kn}}, \tag{B1}$$

and

$$\mathrm{C}_4^{\mathrm{NSF}^2} = -\wp\frac{\beta + \sqrt{2\pi}\,\mathrm{Kn} + 2\beta\,\mathrm{Kn}^2}{4\beta\,\mathrm{Kn}}, \tag{B2}$$

where $\beta = \chi/(2-\chi)$.

Similarly, the constants for regularized 13-moment solutions [Eqs. (57b) and (57c)] can be obtained from their boundary conditions (43a) and (43b),

$$\mathrm{C}_2^{\mathrm{R13}} = \wp\frac{4\beta(C\,\mathrm{Pr} - 12)\mathrm{Kn} - 5\sqrt{2\pi}\,\mathrm{Pr}}{\mathrm{Pr}[48\beta\mathcal{J}_0(f) + 10\sqrt{2\pi B_2\,\mathrm{Pr}}\mathcal{J}_1(f)]}, \tag{B3}$$

$$\mathrm{C}_4^{\mathrm{R13}} = -\frac{\wp}{20\beta\,\mathrm{Kn}\,\mathrm{Pr}}\left\{\frac{2\beta[65\sqrt{2\pi}\,\mathrm{Pr}\,\mathrm{Kn} + 60\beta\,\mathrm{Pr} - 4\beta(7C\,\mathrm{Pr} - 24)]\mathrm{Kn}^2\,\mathcal{J}_0(f)}{24\beta\mathcal{J}_0(f) + 5\sqrt{2\pi B_2\,\mathrm{Pr}}\mathcal{J}_1(f)}\right.$$
$$\left. + \frac{5\sqrt{B_2\,\mathrm{Pr}}[10\pi\,\mathrm{Pr}\,\mathrm{Kn} + 5\sqrt{2\pi}\beta\,\mathrm{Pr} - 2\sqrt{2\pi}\beta(C\,\mathrm{Pr} - 2)\mathrm{Kn}^2]\mathcal{J}_1(f)}{24\beta\mathcal{J}_0(f) + 5\sqrt{2\pi B_2\,\mathrm{Pr}}\mathcal{J}_1(f)}\right\}, \tag{B4}$$

with

$$f = \frac{2}{\mathrm{Kn}}\sqrt{\frac{\mathrm{Pr}}{B_2}}.$$

For the thermal transpiration flow the constants read

$$\mathsf{C}_4^{\mathrm{NSF}^1} = \mathsf{C}_4^{\mathrm{N\ SF}^2} = -\tau\frac{\mathrm{Kn}}{2\ \mathrm{Pr}}, \tag{B5}$$

and

$$\mathsf{C}_2^{\mathrm{R13}} = \tau\frac{60\beta\ \mathrm{Kn}}{\mathrm{Pr}[24\beta\mathcal{J}_0(f) + 5\sqrt{2\pi B_2\ \mathrm{Pr}}\mathcal{J}_1(f)]}, \tag{B6}$$

$$\mathsf{C}_4^{\mathrm{R13}} = -\tau\frac{5\sqrt{\pi B_2}\ \mathrm{Kn}\ \mathcal{J}_1(f)}{24\beta\sqrt{2\ \mathrm{Pr}}\mathcal{J}_0(f) + 10\sqrt{\pi B_2}\ \mathrm{Pr}\ \mathcal{J}_1(f)}. \tag{B7}$$

[1] C. Cercignani, *Theory and Application of the Boltzmann Equation* (Scottish Academic, Edinburgh, 1975).
[2] S. Chapman and T. G. Cowling, *The Mathematical Theory of Non-Uniform Gases* (Cambridge University Press, Cambridge, 1970).
[3] H. Grad, "On the kinetic theory of rarefied gases," Commun. Pure Appl. Math. **2**, 325 (1949).
[4] H. Grad, in *Handbuch der Physik*, edited by S. Flügge (Springer, Berlin, 1958), Vol. 12.
[5] A. V. Bobylev, "The Chapman-Enskog and Grad methods for solving the Boltzmann equation," Sov. Phys. Dokl. **27**, 29 (1982).
[6] L. S. García-Colín, R. M. Velasco, and F. J. Uribe, "Beyond the Navier–Stokes equations: Burnett hydrodynamics," Phys. Rep. **465**, 149 (2008).
[7] H. Struchtrup and M. Torrilhon, "Regularization of Grad's 13-moment equations: Derivation and linear analysis," Phys. Fluids **15**, 2668 (2003).
[8] H. Struchtrup, "Stable transport equations for rarefied gases at high orders in the Knudsen number," Phys. Fluids **16**, 3921 (2004).
[9] M. Torrilhon and H. Struchtrup, "Boundary conditions for regularized 13-moment-equations for micro-channel-flows," J. Comput. Phys. **227**, 1982 (2008).
[10] M. Torrilhon and H. Struchtrup, "Regularized 13-moment-equations: Shock structure calculations and comparison to Burnett models," J. Fluid Mech. **513**, 171 (2004).
[11] H. Struchtrup and T. Thatcher, "Bulk equations and Knudsen layers for the regularized 13 moment equations," Continuum Mech. Thermodyn. **19**, 177 (2007).
[12] P. Taheri, M. Torrilhon, and H. Struchtrup, "Couette and Poiseuille microflows: Analytical solutions for regularized 13-moment equations," Phys. Fluids **21**, 017102 (2009).
[13] H. Struchtrup and M. Torrilhon, "Higher-order effects in rarefied channel flows," Phys. Rev. E **78**, 046301 (2008).
[14] P. Taheri, A. S. Rana, M. Torrilhon, and H. Struchtrup, "Macroscopic description of steady and unsteady rarefaction effects in boundary value problems of gas dynamics," Continuum Mech. Thermodyn. **21**, 423 (2009).
[15] P. Taheri and H. Struchtrup, "Effects of rarefaction in microflows between coaxial cylinders," Phys. Rev. E **80**, 066317 (2009).
[16] F. Sharipov and V. Seleznev, "Data on internal rarefied gas flows," J. Phys. Chem. Ref. Data **27**, 657 (1998).
[17] C. Cercignani and F. Sernagiotto, "Cylindrical Poiseuille flow of rarefied gas," Phys. Fluids **9**, 40 (1966).
[18] J. H. Ferziger, "Flow of a rarefied gas through a cylindrical tube," Phys. Fluids **10**, 1448 (1967).
[19] M. Knudsen, "Eine revision der gleichgewichtsbedingung der gase. thermische molekularströmun," Ann. Phys. **31**, 205 (1910).
[20] Y. Sone and K. Yamamoto, "Flow of rarefied gas through a circular pipe," Phys. Fluids **11**, 1672 (1968).
[21] S. K. Loyalka, "Thermal transpiration in a cylindrical tube," Phys. Fluids **12**, 2301 (1969).
[22] O. Reynolds, "Experimental researches on thermal transpiration of gases through porous plates and on the law of transpiration and impulsion," Philos. Trans. R. Soc. London **170**, 727 (1879).
[23] M. Knudsen, "Thermischer molekulardruck der gase in Röhren," Ann. Phys. **338**, 1435 (1910).
[24] Y. Sone, *Kinetic Theory and Fluid Dynamics* (Birkhäuser, Boston, 2002).
[25] F. Sharipov, "Rarefied gas flow through a long tube at any temperature ratio," J. Vac. Sci. Technol. A **14**, 2627 (1996).
[26] F. Sharipov, "Application of the Cercignani–Lampis scattering kernel to calculations of rarefied gas flows. III. Poiseuille flow and thermal creep through a long tube," Eur. J. Mech. B/Fluids **22**, 145 (2003).
[27] S. Varoutis, D. Valougeorgis, O. Sazhin, and F. Sharipov, "Rarefied gas flow through short tubes into vacuum," J. Vac. Sci. Technol. A **26**, 228 (2008).
[28] H. Struchtrup, *Macroscopic Transport Equations for Rarefied Gas Flows* (Springer, New York, 2005).
[29] C. Maxwell, "On stress in rarefied gases arising from inequalities of temperature," Philos. Trans. R. Soc. London **170**, 231 (1879).
[30] X. Gu and D. Emerson, "A computational strategy for the regularized 13 moment equations with enhanced wall-boundary conditions," J. Comput. Phys. **225**, 263 (2007).
[31] S. K. Loyalka, "Kinetic theory of thermal transpiration and mechanocaloric effect. I," J. Chem. Phys. **55**, 4497 (1971).
[32] S. K. Loyalka, "Kinetic theory of thermal transpiration and mechanocaloric effect. II," J. Chem. Phys. **63**, 4054 (1975).
[33] D. Valougeorgis and J. R. Thomas, "Exact numerical results for Poiseuille and thermal creep flow in a cylindrical tube," Phys. Fluids **29**, 423 (1986).
[34] C. E. Siewert, "Poiseuille and Thermal-creep flow in a cylindrical tube," J. Comput. Phys. **160**, 470 (2000).
[35] G. A. Bird, "Definition of mean free path for ideal gases," Phys. Fluids **26**, 3222 (1983).
[36] C. E. Siewert and D. Valougeorgis, "An analytical discrete-ordinates solution of the S-model kinetic equations for flow in a cylindrical tube," J. Quant. Spectrosc. Radiat. Transf. **72**, 531 (2002).
[37] S. K. Loyalka and S. A. Hamoodi, "Poiseuille flow of a rarefied gas in a cylindrical tube: Solution of linearized Boltzmann equation," Phys. Fluids A **2**, 2061 (1990).
[38] S. S. Lo and S. K. Loyalka, "An efficient computation of near-continuum rarefied gas flows," Z. Angew. Math. Phys. **33**, 419 (1982).
[39] B. T. Porodnov, A. N. Kulev, and F. T. Tukhvetov, "Thermal transpiration in a circular capillary with a small temperature difference," J. Fluid Mech. **88**, 609 (1978).
[40] B. T. Porodnov and F. T. Tukhvetov, "Theoretical investigation of nonisothermal flow of a rarefied gas in a cylindrical capillary," J. Eng. Phys. Thermophys. **36**, 61 (1979).
[41] S. S. Lo, S. K. Loyalka, and T. S. Storvick, "Kinetic theory of thermal transpiration and mechanocaloric effect. V. Flow of polyatomic gases in a cylindrical tube with arbitrary accommodation at the surface," J. Chem. Phys. **81**, 2439 (1984).
[42] S. R. De Groot and P. Mazur, *Non-Equilibrium Thermodynamics* (Dover, New York, 1984).
[43] F. Sharipov, "Onsager-Casimir reciprocity relations for open gaseous systems at arbitrary rarefaction: I. General theory for single gas," Physica A **203**, 437 (1994).
[44] F. Sharipov, "Onsager-Casimir reciprocity relations for open gaseous systems at arbitrary rarefaction: II. Application of the theory for single gas," Physica A **203**, 457 (1994).
[45] P. Taheri and H. Struchtrup, "Rarefaction effects in thermally-driven microflows," Physica A **389**, 3069 (2010).
[46] X. Gu and D. R. Emerson, "A high-order moment approach for capturing non-equilibrium phenomena in the transition regime," J. Fluid Mech. **636**, 177 (2009).